The mode of incorporation of As(-I) and Se(-I) in natural pyrite revisited

Alain Manceau, Margarita Merkulova, Olivier Mathon, Pieter Glatzel, Magdalena Murdzek, Valentina Batanova, Alexandre Simionovici, Stephan N. Steinmann, Dogan Paktunc

The mode of incorporation of As(-I) and Se(-I) in natural pyrite revisited

Alain Manceau[*1], *Margarita Merkulova*[*2,§], *Olivier Mathon*[2], *Pieter Glatzel*[2], *Magdalena Murdzek*[2], *Valentina Batanova*[1], *Alexandre Simionovici*[1], *Stephan N. Steinmann*[3], *Dogan Paktunc*[4]

[1]Univ. Grenoble Alpes, CNRS, ISTerre, CS 40700, 38058 Grenoble, France

[2]European Synchrotron Radiation Facility (ESRF), 71 Rue des Martyrs, 38000 Grenoble, France

[3]Univ. Lyon, ENS de Lyon, CNRS, Laboratoire de Chimie, 69342 Lyon, France

[4]Nat. Resources Canada, CanmetMINING, 555 Booth St, Ottawa, ON, Canada

[§]Present address: Department of Geology, University of Liege, B-4000 Liege, Belgium

Corresponding Authors :

alain.manceau@univ-grenoble-alpes.fr

margarit.merkulova@gmail.com

Key words: arsenic, selenium, EXAFS, XANES, Crystal14, ab initio, DFT

ABSTRACT: Pyrite (FeS_2) from coal, sedimentary rocks, and hydrothermal ore deposits generally contains hazardous selenium (Se) and arsenic (As) that are released in natural waters through oxidative dissolution of the host. Knowing how As and Se are structurally incorporated into pyrite has important implication in controlling or preventing their release because trace metal(loid) substitution accelerates the dissolution of pyrite. Previous extended X-ray absorption fine structure (EXAFS) studies have reported that nominally monovalent arsenic clusters at the sulfur site forming As-As pairs at 3.2 Å, whereas monovalent Se does not form Se-Se pairs at this distance for unknown reason. Here, we revisit this question using As and Se K-edge X-ray absorption near-edge structure (XANES) and EXAFS spectroscopy complemented with atomistic calculations. We find that neither As nor Se atoms can be differentiated from S atom at 3.2-3.3 Å, the cluster and dilute model-fits to As- and Se-EXAFS data yielding equivalent least-squares solutions. Thermodynamic calculations of $Fe_{48}As_3S_{93}$ (3.8 wt.% As) and $Fe_{48}Se_3S_{93}$ (4.0 wt.% Se) structures show that the formation of As-As pairs is energetically favorable and the formation of Se-Se pairs unfavorable. Thus, the equilibrium distribution of As and Se predicted by calculation agrees with published EXAFS data. However, this agreement is incidental because EXAFS fits are ambiguous, the same EXAFS spectra being fit indifferently with a cluster and

a dilute model. Regarding Se, the dilute model-fit is probably correct since Se-Se pairs are precluded thermodynamically. The situation is less clear for As. The lowest energy atomic arrangement of As in $Fe_{48}S_{93}As_3$ is similar to the local structure of As in arsenopyrite (FeAsS), thus supporting the cluster model. However, the energy gain to total energy provided by the formation of As clusters decreases with decreasing As concentration, making them thermodynamically less favorable below 1.0 wt.%.

INTRODUCTION

Arsenic and selenium often substitute for sulfur in pyrite (FeS_2). Arsenic commonly amounts to several thousand mg/kg FeS_2 (ppm) in sedimentary pyrite,[1-7] and can reach up to 10-20 weight-percent (wt.%) in gold deposits.[8-10] The As-Au association has been described in hydrothermal, epithermal, porphyry Cu and Au, Carlin-type and massive volcanogenic gold deposits.[9, 11, 12] In contrast, Se rarely exceeds a few hundred mg/kg. Selenious pyrite (Se-pyrite) occurs most frequently in coal[13-16] and shale[17, 18] rocks.

The crystal chemistry of As and Se in pyrite has attracted much interest in the last two decades for economic and environmental reasons. Pyrite often contains valuable metals, such as Ni, Cu, Sb, and Ag, in addition to Au, and their concentrations are broadly correlated with As.[12, 19-21] However, the mining and smelting of sulfide ores and the processing and combustion of coal release hazardous metal(loid)s, including Hg and Tl besides As and Se.[22-33] It is important to know the modes of incorporation of As and Se in pyrite and their association with trace elements at the atomic scale to recover efficiently and safely valuable metals and to develop better methods of sulfide ore roasting, coal cleaning, and mine waste management.

As and Se have a nominal oxidation state of 1- in FeS_2 and substitute for sulfur in the S_2^{2-} dianion units which coordinate Fe in the pyrite crystal structure (Figure 1a).[34-38] On the basis of their chemical similarity, one would expect As and Se to have similar local structure and atomic distribution. However, As-EXAFS and Se-EXAFS studies on natural pyrite have concluded otherwise.

Savage et al.[36] analyzed an arsenian pyrite (As-pyrite) of average composition $FeAs_{0.02}S_{1.98}$ (1.2 wt.% As) from gold mineralization using As-EXAFS spectroscopy. EXAFS data were fit with one S atom at 2.25 Å in the first coordination shell ($[AsS]_1$), and 4 S atoms at 3.10 Å ($[AsS]_2$) and 3 As atoms at 3.17 Å ($[AsAs]_2$) in the second anionic shell (Figure 1a). The authors concluded that As occurs in clusters in pyrite and explained the lack of detection of $[AsAs]_1$ pairs to the close proximity of 3 $[AsFe]_1$ pairs at 2.32 Å. The lack of $[AsAs]_1$ pairs is consistent with density functional theory (DFT), which predicts that the $AsAs^{2-}$ unit is energetically less favorable than the AsS^{2-} unit.[39] Nanoinclusion

of arsenopyrite (FeAsS), which has $[AsS]_1$ and $[AsAs]_2$ pairs in its structure (Figure 1b), was excluded from EXAFS and HRTEM imaging. As clustering in the second S shell around a central As atom was confirmed by Paktunc[35] in arsenian pyrite from Carlin-type gold deposit containing 1.5 mol per cent As ($FeAs_{0.03}S_{1.97}$; 1.6 wt.% As). EXAFS data were fit with 3 $[AsAs]_2$ pairs at 3.24 Å and 2 $[AsS]_2$ pairs at 3.34 Å. The two studies agree with ab initio thermodynamic calculations, which show that pyrite can host up to ~6 wt.% of As ($FeAs_{0.10}S_{1.90}$) in solid solution before unmixing into pyrite-arsenopyrite domains.[40] A compositional segregation of As atoms at a mean concentration of only 1.0 mol per cent As ($FeAs_{0.02}S_{1.98}$) was, however, unexpected because no $FeAs_2$ mineral isostructural to cubic FeS_2 is known.

Ryser et al.[17] analyzed a Se-pyrite grain containing as much as 0.7 wt.% Se ($FeSe_{0.01}S_{1.99}$) from a mine-waste rock shale using micro XANES and EXAFS spectroscopy. They concluded that Se forms $[SeSe]_1$ pairs at 2.25 Å from the central Se atom and 12 $[SeS]_2$ pairs at 3.24 Å. Matamoros-Veloza et al. [18], who also studied a shale pyrite by X-ray microspectroscopy but containing ten times less Se (about 600 ppm), fit the EXAFS spectrum from euhedral grain with a $[SeS]_1$ pair at 2.34 Å and 6 $[SeS]_2$ pairs at 3.20 Å. The two model-fits for Se-pyrite agree in next-nearest neighbor identities, but not in nearest. The Se atoms are dispersed locally in the second study and clustered in the nearest S sites in the first study. Se_2^{2-} dianion units in Se-pyrite are structurally possible because cubic $FeSe_2$, named dzharkenite, occurs naturally in solid solution with pyrite.[41]

EXAFS results obtained on As- and Se-pyrite raise several questions. Why would Se form $[SeSe]_1$ pairs in the nearest S sites and not the next-nearest, and how $[SeSe]_1$ pairs can form at a Se/S atomic ratio of $0.01/1.99 = 5 \times 10^{-3}$? Does it mean that $SeSe^{2-}$ units are more stable than SeS^{2-} units, in contrast to the $AsAs^{2-}$ and AsS^{2-} units? Why is As locally clustered in the next-nearest S sites at an As/S atomic ratio of 0.02/1.98 = 0.01, but not Se at similar Se/S ratio? Here, we address these questions by combining electron microprobe (EPMA) and synchrotron-based X-ray microfluorescence (SXRF) analysis and As and Se K-edge high energy-resolution XANES (HR-XANES) and EXAFS spectroscopy with quantum-mechanical calculations. Five pyrite specimen were studied, two at the As-edge from hydrothermal veins, two at the As- and Se-edge from epithermal and sedimentary deposits, and one at the Se-edge only from another sedimentary deposit.

MATERIALS AND METHODS

The origin and geological setting of the five pyrite are listed in Table 1. Four specimen (Bol, Ger, Sp, Sw) are massive aggregates of pyrite crystals and one (Ut) is a centimeter-sized single crystal

(Figure S1). Mineralogical purity was verified by X-ray diffraction (Figure S2). The distributions of As and Se were imaged and their point concentrations measured on polished sections by EPMA using a JEOL JXA-8230 microprobe equipped with five wavelength-dispersive spectrometers (WDS) and an energy-dispersive spectrometer (EDS).[42] As in pyrite Ut and Ger was analyzed also by ICP-AES and Se by ICP-MS to verify the consistency between point and bulk analyses.

Parts of the samples were ground into powder in a glove bag filled with He to prevent oxidation and the powder was pressed into pellets for bulk HR-XANES and EXAFS measurements. HR-XANES data were acquired on beamline ID26 at the European Synchrotron Radiation Facility (ESRF, Grenoble) using a multi-crystal analyzer spectrometer.[43] EXAFS data were acquired on beamline BM23 in fluorescence-yield mode using a silicon drift diode detector (SDD). Bulk As-EXAFS was measured on pyrite Bol and Se-EXAFS on pyrite Ut. Growth zones with a wide range of As-Au concentrations were imaged by EPMA in pyrite Bol. A zoned area was relocated by micro SXRF and four As K-edge micro EXAFS spectra were acquired on spots differing in As concentration. The laterally resolved measurements were performed on the microprobe endstation of beamline BM23.[44] The incident beam was focused to 5x5 μm^2 with a set of Pt-coated Kirkpatrick-Baez (K-B) mirrors.

The absolute energy of the HR-XANES spectra is referenced at the As and Se K-edges to the first maximum of the derivative (inflection point) taken to 11870.0 eV for As_2O_3 and to 12658.0 eV for elemental Se (Se^0).[17] The precision of the energy is ± 0.1 eV. The reference compounds arsenopyrite (FeAsS) and realgar (As_4S_4) at the As edge, and ferroselite (orthorhombic $FeSe_2$), achavelite (FeSe), elemental Se, Na_2SeO_3, and Na_2SeO_4 at the Se edge, were diluted to 500 ppm in boron nitride (BN) to prevent overabsorption.[45] Additional methodological information (XRD, ICP-ES/MS, EPMA, XANES, EXAFS) is provided in the Supporting Information (SI).

Atomistic models of As and Se incorporation in pyrite were constructed with DFT using the CRYSTAL14[46] code for periodic systems, and a computational methodology adapted from Smith et al.[47, 48] The hybrid PWGGA functional PW1PW with 20% HF contribution[49] was used for all calculations. The PBEsol0 functional, a hybrid version of the PBEsol XC functional comprising 25% Hartree-Fock (HF) exchange,[50] was used as a check on the reliability of the PW1PW functional. The all-electron split-valence 6-311G Pople's basis set[51] was employed for S. An effective core pseudopotential with s411p411d411 external shell was used for Fe[52] in pyrite models doped with As. The TZVP basis set of triple-zeta valence quality with polarization functions was employed for Fe[53] in Se-pyrite models. The As and Se atoms were described with an effective core pseudopotential and the m-pVDZ double-zeta valence with polarization functions basis set.[54]

The PW1PW and PBEsol0 functionals and basis sets were benchmarked by calculating the ionization energies of Fe, S, As and Se (Tables S1-S4), and by assessing the precision of the lattice parameters calculated on single unit cells of known structures (Tables S5-S7). The lattice parameters and interatomic distances derived from our modeling procedure (PW1PW functional) deviate from crystallographic values at most by 1.9% and 2.3% for pyrite,[2] 1.7% and 2.7% for marcasite (orthorhombic FeS_2),[2] 0.8% and 1.9% for arsenopyrite (FeAsS),[55] 1.4% and 2.5% for löllingite (orthorhombic $FeAs_2$),[56] 0.16% and 5.03% for dzharkenite (cubic $FeSe_2$)[57] (Tables S8-S14). The errors are typical of DFT GGA studies.[39, 58-60] The distributions of As and Se were modeled in two supercells of dimensions 2 x 2 x 2 and 3 x 2 x 2. The reciprocal space integration was performed by sampling the Brillouin zone with the 6 x 6 x 6 Pack-Monkhorst mesh,[61] resulting in 112 independent *k* points. Parameter space testing and tolerances for Coulomb and exchange sums are reported in Tables S15-17. Additional computational information is provided in SI.

RESULTS AND DISCUSSION

Distribution and concentration of As and Se. Backscattering electron imaging and EPMA mapping show that As and Se are uniformly distributed within the grains of pyrite Ger, Sp, Sw, and Ut (Figure 2). They are free of As- and Se-containing inclusions, such as goldfieldite and colusite sulfide inclusions reported in hydrothermal pyrite.[62] Pyrite Sp contains minute inclusions of chalcopyrite ($CuFeS_2$) observed as brighter scattering spots on backscattered electron images. The four pyrite cover a large range of As and Se concentrations (Table 1). As content varies from below the EPMA detection limit of 23 ppm (Sp) to 1590 ppm (Ger), and Se content from below the detection limit of 34 ppm (Sp and Sw) to a maximum of 428 ppm (Ut). Although uniform at the grain scale, As and Se contents vary from grain to grain. As content varies from the detection limit of 23 ppm to 60 ppm in Sw based on the analysis of five grains, and from 50 ppm to 160 ppm in Ut based on the analysis of three grains. Similarly, Se content varies from 318 ppm to 428 ppm in Ut based on three grain analyses.

Growth-zoning compositional variations are observed on the BSE image and EPMA maps of pyrite Bol (Figure S3). On the basis of eight point analyses, As content among the zones varies between 0.15 and 1.14 wt.%, and Se content varies from below the detection limit of 34 ppm to 70 ppm (Table 1). Scatter plots of the fluorescence counts between two elements were derived from each pixel of the EPMA maps, and the co-occurrence between two elements was evaluated from the linear Pearson correlation coefficient ρ. Elemental scatter analysis shows that As and Se are negatively correlated

with S (ρ(As-S) = -0.84, ρ(Se-S) = -0.64), and positively correlated together (ρ(As-Se) = 0.67) (Figure S4). Gold (Au) was detected at a concentration of 60 ppm in one spot out of the eight analyzed (detection limit = 47 ppm). The distribution of Au is heterogeneous within pyrite, being localized in growth bands enriched in As (Figure S3). Scatter analysis shows that Au is, however, weakly correlated to As and Se (ρ(As-Au) = 0.29, ρ(Se-Au) = 0.22) and not to Fe (ρ = -0.01). Elemental correlations have limited chemical significance here, because Au is about three orders of magnitude less concentrated than As and more than four orders less than Fe. Analytical precision is not sufficient to calculate ρ confidently. In addition, the Au and Se fluorescence counts on the EPMA maps represent noise when point concentrations are below the detection limit. These points on the As-Au and Fe-Au correlation plots bias the ρ value. We conclude that the strong negative correlation between abundant As (0.15 – 1.14 wt.%) and major S (ρ(As-S) = -0.84) is evidence for As substitution at the S site. Se probably replaces also S, the lower Pearson correlation (ρ(Se-S) = -0.64) being attributed to the lower Se content, and larger ρ uncertainty thereof.

Formal oxidation state and local structure of As and Se from HR-XANES. Pyrite Bol, Sw, Ut, and Sp were measured at the As K-edge and pyrite Ut, Sp, and Ger at the Se K-edge. The As absorption white line is at 11866.2 eV and the Se white line at 12658.4 eV for all pyrites (Figures 3a and 3b). These edge energies are in the range of those for reduced As and Se compounds and several electronvolts lower than the K edges of oxidized As and Se species (Figures 3c and 3d, Tables S18 and S19). Of the reference spectra, those of arsenopyrite (FeAsS) at the As edge and of arsenopyrite (2 ppm Se) and marcasite (orthorhombic FeS_2, 12 ppm Se) at the Se K-edge provided the best match to the pyrite spectra, confirming the nominal -1 oxidation state of both As and Se in pyrite (Figures 4a-c). Comparison of the pyrite and reference spectra identifies three "indicator" features denoted A, B, and C in Figure 4a.

Region A refers to the energy of the white line. The As edge is at 11865.9 eV for arsenopyrite and 11866.2 eV for pyrite, and the Se edge is at 12657.8 eV for arsenopyrite, 12658.2 eV for marcasite, and 12658.4 eV for pyrite. Region B is situated 32-42 eV above the edge. The pyrite spectra show an absorption hump at this place, which is absent in arsenopyrite and marcasite. The edge energy and structure differences make it possible to distinguish a pyrite host with a corner-linked framework and cubic structure, from arsenopyrite and marcasite with a chain framework and a lower symmetry crystallographic structure (Figure 1). This finding was verified by calculating ab initio the arsenopyrite, marcasite, and pyrite spectra with the finite difference method (FDM) as implemented in FDMNES.[63]

The code calculates the final state potential in real space from a cluster of atoms. The form of the potential is not approximated, in contrast to the alternative muffin-tin approach, [64, 65] thus providing a better description of scattering phenomena. The As and Se clusters had a radius of 7 Å and were built from crystallographic structures[2, 55] by replacing S and As with As and Se at the center (As pyrite, Se pyrite, Se marcasite, and Se arsenopyrite). Relaxation of the As and Se sites with CRYSTAL14 did not change the results. Figures 4d-f show that the two XANES fingerprints, edge energy and absorption hump, of As and Se substitution at the S site in pyrite are reproduced theoretically.

Region C is situated 8 eV above the edge energy and corresponds to the first absorption structure after the white line. As-XANES of pyrite has a higher absorption amplitude at 11874.0 eV relative to arsenopyrite. The increase in amplitude is particularly noticeable for Ut (Figure 3a). The energy value of this feature is close to the edge energy of As_2O_5 (11873.6 eV), which suggests that Ut at least, and perhaps all pyrites, contain some As(V). This species is attributed to the oxidation of arsenic exposed on the surface of pyrite grains.[35]

Local structure of As and Se from EXAFS. Bulk EXAFS spectra measured at the As (pyrite Bol) and Se (pyrite Ut) K-edges are essentially the same, differing only in the amplitude of the oscillations at $k < 4$ Å^{-1} and $k = 10$ Å^{-1} (Figure 5a). They have the same frequency and structure, meaning that As and Se have similar short range order in pyrite. Comparison with the EXAFS spectrum of arsenopyrite (FeAsS) shows that the local coordination of As in this mineral does not replicate that of As and Se in pyrite, in agreement with HR-XANES (Figure 5b). Because Bol is zoned, four micro As-EXAFS spectra were measured at points of interests (POI) selected from the micro As-SXRF map (Figure S5a). There is a factor of three in count rate between the richest (spot 6) and the least (spot 8) As-rich point (Figure S5b). The four spectra have the same frequency and structure and they average out to the bulk spectrum (Figure S6). Thus, zoning reflects varying geochemical conditions during crystallization and does not appear to correlate with the chemical form of As.

Careful study of the As-pyrite spectra from Savage et al. (Clio-2 sample)[36] and Paktunc et al. (grain 218)[35], and the two Se-pyrite spectra from Matamoros-Veloza et al. (POI*a*,*b*)[18] indicates a considerable degree of similarity with our spectra. Since the EXAFS spectra in the previous studies were fit with S atoms in the first shell (i.e., $[AsS]_1$ and $[SeS]_1$ pairs), this infers that As and Se are also bonded to S in our samples. Although this consistency check shows good agreement among different studies in the first anionic shell analysis of As and Se, discrepancies exist in the analysis of the second anionic shell. Savage et al.[36] and Paktunc[35] concluded that As is clustered forming $[AsAs]_2$ pairs,

whereas Matamoros-Veloza et al. (POI*a*,*b*)[18] observed $[SeS]_2$ pairs only. How can two EXAFS spectra that look similar (i.e., As-pyrite and Se-pyrite) lead to distinct results? We show below that the As- and Se-EXAFS spectra have two least-squares minima in the parameter space.

To obtain robust structural solutions, care was taken to not overparametrize the model-fits. The limit of the number of free parameters in EXAFS fits can be calculated by the Nyquist formula $N = (2\Delta R\Delta k)/\pi$. Nine parameters were adjusted (Table 2), for a number of degrees of freedom in the refinements of $N = [(2 \times (16.0 - 2.7\ \text{Å}^{-1}) \times (3.6 - 1.4\ \text{Å})]/\pi = 18.6$ for As-pyrite and $N = [(2 \times (13.8 - 3.4\ \text{Å}^{-1}) \times (3.6 - 1.4\ \text{Å})]/\pi = 14.6$ for Se-pyrite. Figures 6 and 7 show that the As- and Se-EXAFS spectra can be fit indifferently with a dilute (model 1) and a cluster (model 2) model. In model 1, As and Se are surrounded by 5.9-6.5 S_2 at 3.08-3.09 Å and 5.5-6.1 S_2 at 3.33 Å, and in model 2 by 6.3-6.6 S_2 at 3.15-3.16 Å and 4.4-5.7 As_2/Se_2 at 3.16 Å. The metric parameters of the S_1, Fe_1, and Fe_2 shells around As and Se are practically identical in the two models (Table 2). Also included in Figures 6 and 7 are the residual of each fit, which indicates the portion of the spectra unfit by the structural model; the lower the residual, the better the fit. The overlay plots of the fit residuals for each model are identical, therefore the two models are equivalent. Consideration of As or Se in the first shell (i.e., As_2^{2-} or Se_2^{2-} dianions) resulted in the fit residual being more than doubled (model 3 in Figures 6 and 7). The As-S_1 distance is 2.27 Å and the Se-S_1 distance is 2.24 Å, compared to the S-S_1 distance of 2.16 Å in pyrite (Table 2). The differences in bond length match the difference of atomic size between S (1.03 Å), As (1.20 Å), and Se (1.16 Å).

In pyrite, the S_2 shell is split into two sub-shells at 3.08 Å and 3.33 Å. In model 1, the two S_2 distances remain unchanged relative to pyrite while the S_1, Fe_1 and Fe_2 distances are relaxed as a result of the As and Se for S substitution. In model 2, the S_1, Fe_1, S_2, and Fe_2 distances are relaxed and an As_2/Se_2 shell at 3.16 Å is detected at the same distance as the S_2 shell. This local structure is not unrealistic because the As distances to smaller S_2 atoms are not shorter on average than the As distances to bigger As_2 atoms in arsenopyrite (FeAsS).[55] Note that EXAFS does not preclude longer As-As and Se-Se distances at about 3.4 Å from existing, but it does not have the sensitivity to detect them. We conclude that the dilute and cluster models are equiprobable from the standpoint of EXAFS analysis. Since EXAFS cannot answer if As and Se are segregated at the local scale, this possibility is examined next by quantum chemical computations.

Equilibrium segregation of As and Se in pyrite. Twelve unique cases of As incorporation schemes and eight unique cases of Se incorporation schemes were tested in total (Figures 8 and S7).

Their total and relative energies with respect to the least favorable configuration are given in Table 3, with the lattice parameters being reported in Table S20 and Cartesian coordinates in the SI. Formation of As_2^{2-} and Se_2^{2-} dianions (i.e., $[AsAs]_1$ and $[SeSe]_1$ pairs) is energetically unfavorable by more than 35 meV/cell (6 kcal/mol, models 2Se-2, 3Se-2, 2As-2, 3As-2). The As-As avoidance in the first S shell had been predicted by Blanchard et al.[39] using DFT. Our results show that this theoretical prediction holds for the $[SeSe]_1$ pair. The equilibrium segregation of As and Se in the second S shell was examined by substituting two As/Se atoms for sulfur in a 2 x 2 x 2 supercell ($Fe_{32}(As/Se)_2S_{62}$), and three As/Se atoms for sulfur in a 3 x 2 x 2 supercell ($Fe_{48}(As/Se)_3S_{93}$). The two models have an (As/Se)/S atomic ratio of 0.03, an As concentration of 3.8 wt.%, and a Se concentration of 4.0 wt.%. The FeS_6 octahedra have six short S-S edges of 3.08 Å in length and six long S-S edges of 3.32Å in length (Figure 1a).[2] Distribution of the As/Se atoms on the long and short edges was varied to examine the energetic preference for clustering on either edge dimension (Figure 8). The main results of this broad evaluation of energy structures are the following:

- As tends to cluster in the second S shell, but not Se, regardless of the number and position of the $[SeSe]_2$ pairs on octahedral edges.
- A cluster of 3 As atoms is energetically more favorable than a cluster of 2 As atoms (e.g., models 3As-3 and 3As-5).
- A cluster of 3 As atoms grouped on the same octahedral face, forming an $[As]_3$ triad as in arsenopyrite (Figure 1b), is energetically more favorable than a cluster of 3 As atoms distributed over two octahedral faces (e.g., models 3As-5 and 3As-7).
- Energies of the 3As models show a monotonic trend in function of the dimension of the S-S edge. Larger energy changes (i.e., higher stability) occur for models in which As atoms are distributed on both short and long S-S edges (e.g., models 3As-4, 3As-5, and 3As-6, and models 3As-7 and 3As-8).
- The As-As distances in the second lowest energy structure (model 3As-7) are 3.07 Å, 3.15 Å, and 3.33 Å, close in value to the arsenopyrite $[As]_3$ triad distances of 3.04 Å, 3.19 Å, and 3.34 Å.[55] Model 3As-7 differs by 6 meV/cell from the lowest energy model 3As-8.

Generation of the local order of As in arsenopyrite engenders confidence in the calculations. Also, the fact that the $[As]_3$ arrangement was not found for Se is consistent with the lack of selenious compound structurally analog to arsenopyrite (i.e., FeSeS). Our results also disallow the coexistence of $[SeSe]_1$ and $[SeSe]_2$ pairs, and of $[SeSe]_1$ and $[SeS]_2$ pairs, in pyrite. $[SeSe]_1$ and $[SeSe]_2$ pairs occur in the pyrite isomorph dzharkenite (cubic $FeSe_2$), and therefore can be expected to be energetically

favorable in selenious pyrite. Our results simply suggest that cubic FeS_2 and $FeSe_2$ are not miscible at the atomic scale. This finding may explain why the two compounds do not form a complete solid-solution at the macroscopic scale,[41] the two structures being in this case intergrown at the microscopic scale.

The absence of $[SeSe]_1$ + $[SeS]_2$ pairs in our models conflicts with the results of Ryser and co-workers,[17] who observed their co-existence in a pyrite grain using EXAFS (POI *g* spectrum). On the basis of our results, if Se occurs in the first S shell, then it should also occur in the second S shell to form an $FeSe_2$ local structure. The $FeSe_2$ hypothesis can be dismissed because the POI *g* spectrum differs from that of dzharkenite. Therefore, the alternative consists of hypothesizing that S atoms, not Se, are present in the first shell. This ambivalence was tested by reanalyzing the Se_1 + Fe_1 contribution to EXAFS for POI *g*. Results reproduced in Figure S8 show that the model-fit of Ryser and co-workers[17] is overparametrized, thus the mathematical solution non-unique. When physically meaningful structural constraints are enforced to suppress correlations between parameters, S atoms give a better fit to data than Se atoms. This is in line with Matamoros-Veloza et al.,[18] who fit their pyrite data with a $[SeS]_1$ pair. We conclude that there is a generally good agreement between theoretical predictions and experiments for Se. Se atoms do not cluster in pyrite at the investigated Se/S ratio ≤ 0.03 (4.0 wt.%), and are predicted to demix as cubic $FeSe_2$ if they do at a higher molar ratio.

In contrast to Se, the lowest energy structures are those in which As occurs in pairs and triads. Formation of an $[As]_3$ triad in a 3 x 2 x 2 supercell allows an energy gain of 41-47 meV/cell or 5-6 meV per sulfur atom (models 3As-7 and 3As-8). The energy change will be lower, the larger the supercell. Therefore, an $[As]_3$ triad is energetically less likely to form at As/S ≤ 0.03 ([As] ≤ 3.8 wt.%), as in the pyrite samples studied by Paktunc[35] (As/S = 0.015, [As] = 1.6 wt.%), Savage[36] (As/Fe = 0.010; [As] = 1.2 wt.%), and here ($0.001 \leq$ As/S ≤ 0.01; 0.15 wt.% $\leq$ [As] ≤ 1.14 wt.%). Arsenic clusters may also form a metastable solid-solution at the nanometer scale precipitated far from thermodynamic equilibrium. Compositional growth zones in pyrite crystals are in fact metastable, and arsenic may very well be inhomogeneously distributed from the micrometer down to the nanometer scale.

The tendency of As to form arsenopyrite-type clusters provides general insights into the dissolution of arsenian pyrite in acid mine drainage. Bioleaching of pyrite and arsenopyrite flotation concentrate shows that arsenopyrite is the first mineral phase to be oxidized, pyrite dissolution starting at a later stage.[66] Further, energetics calculation predicts that As for S substitution promotes the

dissolution of pyrite.[39] Therefore, the presence of arsenopyrite-type clusters should enhance pyrite dissolution even further with the environmental implications that ensue.

In conclusion, this study highlights a previously unknown limitation of EXAFS spectroscopy for the study of As and Se in sulfide minerals, which warrants the utmost caution in drawing fine structural distinctions. We showed that $SeSe^{2-}$ dianionic pairs are unlikely to exist unless Se is clustered as $FeSe_2$ nanoinclusions in the FeS_2 framework. In this case, $[SeSe]_1$ pairs coexist with $[SeSe]_2$ pairs and Fe is bonded to six Se atoms. Arsenic clusters are thermodynamically easier to form than Se clusters, because of the existence of the FeAsS phase. In this case, the lowest energy bonding environment resembles the local structure of FeAsS, in which Fe is bonded to three As atoms on one octahedral face and to three S atoms on the other octahedral face.

ASSOCIATED CONTENT

Supporting Information

The Supporting Information is available free of charge on the ACS Publications website at DOI:

Materials and methods, supplementary tables and figures, EXAFS spectra (PDF)

Cartesian coordinates of the DFT models (XLS)

AUTHOR INFORMATION

Corresponding Authors

E-mail: alain.manceau@univ-grenoble-alpes.fr

E-mail: margarit.merkulova@gmail.com

ORCID

Pieter Glatzel: 0000-0001-6532-8144

Alain Manceau: 0000-0003-0845-611X

Stephan N. Steinmann: 0000-0002-2777-356X

Notes

The authors declare no competing financial interests.

ACKNOWLEDGMENTS

Support was provided by the French National Research Agency (ANR) under grant ANR-10-EQPX-27-01 (EcoX Equipex). The Froggy platform of the CIMENT infrastructure (ANR Grant ANR-10-

EQPX- 29-01) and the ESRF provided computing resources. Pierre Girard and Rainer Wilcke provided their expertise in parallel scientific processing, and Andreas Voegelin from the EAWAG in Zürich provided the arsenopyrite spectrum.

REFERENCES

(1) Smedley, P. L.; Kinniburgh, D. G. A review of the source, behaviour and distribution of arsenic in natural waters. *Appl. Geochem.* **2002,** *17*, 517-568.

(2) Rieder, M.; Crelling, J. C.; Sustai, O.; Drabek, M.; Weiss, Z.; Klementova, M. Arsenic in iron disulfides in a brown coal from the North Bohemian Basin, Czech Republic. *Int. J. Coal Geol.* **2007,** *71*, 115-121.

(3) Jerzykowska, I.; Majzlan, J.; Michalik, M.; Göttlicher, J.; Steininger, R.; Blachowski, A.; Ruebenbauer, K. Mineralogy and speciation of Zn and As in Fe-oxide-clay aggregates in the mining waste at the MVT Zn–Pb deposits near Olkusz, Poland. *Chem. Erde-Geochim.* **2014,** *74*, 393-406.

(4) Stuckey, J. W.; Schaefer, M. V.; Kocar, B. D.; Dittmar, J.; Pacheco, J. L.; Benner, S. G.; Fendorf, S. Peat formation concentrates arsenic within sediment deposits of the Mekong Delta. *Geochim. Cosmochim. Acta.* **2015,** *149*, 190-205.

(5) Biswas, A.; Hendry, M. J.; Essilfie-Dughan, J. Geochemistry of arsenic in low sulfide-high carbonate coal waste rock, Elk Valley, British Columbia, Canada. *Sci. Tot. Environ.* **2016,** *579*, 396-408.

(6) Etschmann, B.; Liu, W. H.; Li, K.; Dai, S. F.; Reith, F.; Falconer, D.; Kerr, G.; Paterson, D.; Howard, D.; Kappen, P., et al. Enrichment of germanium and associated arsenic and tungsten in coal and roll-front uranium deposits. *Chem. Geol.* **2017,** *463*, 29-49.

(7) Wang, Y. H.; Le Pape, P.; Morin, G.; Asta, M. P.; King, G.; Bartova, B.; Suvorova, E.; Frutschi, M.; Ikogou, M.; Pham, V. H. C., et al. Arsenic speciation in Mekong Delta sediments depends on their depositional environment. *Environ. Sci. Technol.* **2018,** *52*, 3431-3439.

(8) Abraitis, P. K.; Pattrick, R. A. D.; Vaughan, D. J. Variations in the compositional, textural and electrical properties of natural pyrite: a review. *Int. J. Miner. Process* **2004,** *74*, 41-59.

(9) Reich, M.; Kesler, S. E.; Utsunomiya, S.; Palenik, C. S.; Chryssoulis, S. L.; Ewing, R. C. Solubility of gold in arsenian pyrite. *Geochim. Cosmochim. Acta* **2005,** *69*, 2781-2796.

(10) Deditius, A. P.; Utsunomiya, S.; Renock, D.; Ewing, R. C.; Ramana, C. V.; Becker, U.; Kesler, S. E. A proposed new type of arsenian pyrite: Composition, nanostructure and geological significance. *Geochim. Cosmochim. Acta* **2008,** *72*, 2919-2933.

(11) Simon, G.; Kesler, S. E.; Chryssoulis, S. Geochemistry and textures of gold-bearing arsenian pyrite, Twin Creeks, Nevada: Implications for deposition of gold in Carlin-type deposits. *Econ. Geol.* **1999,** *94*, 405-421.

(12) Deditius, A. P.; Reich, M.; Kesler, S. E.; Utsunomiya, S.; Chryssoulis, S. L.; Walshe, J.; Ewing, R. C. The coupled geochemistry of Au and As in pyrite from hydrothermal ore deposits. *Geochim. Cosmochim. Acta* **2014,** *140*, 644-670.

(13) Lussier, C.; Veiga, V.; Baldwin, S. The geochemistry of selenium associated with coal waste in the Elk River Valley, Canada. *Environ. Geol.* **2003,** *44*, 905-913.

(14) Diehl, S. F.; Goldhaber, M. B.; Koenig, A. E.; Lowers, H. A.; Ruppert, L. F. Distribution of arsenic, selenium, and other trace elements in high pyrite Appalachian coals: Evidence for multiple episodes of pyrite formation. *Int. J. Coal Geol.* **2012,** *94*, 238-249.

(15) Kolker, A. Minor element distribution in iron disulfides in coal: A geochemical review. *Intern. J. Coal Geol.* **2012,** *94*, 32-43.

(16) Hendry, M.; Biswas, A.; Essilfie-Dughan, J.; Chen, N.; Day, S. Reservoirs of Selenium in Coal Waste Rock, Elk Valley, British Columbia, Canada. *Environ. Sci. Technol.* **2015,** *49*, 8228-8236.

(17) Ryser, A. L.; Strawn, D. G.; Marcus, M. A.; Johnson-Maynard, J. L.; Gunter, M. E.; Moller, G. Micro-spectroscopic investigation of selenium-bearing minerals from the Western US Phosphate Resource Area. *Geochem. Trans.* **2005,** *6*, 1-11.

(18) Matamoros-Veloza, A.; Peacock, C. L.; Benning, L. G. Selenium speciation in framboidal and euhedral pyrites in shales. *Environ. Sci. Technol.* **2014,** *48*, 8972-8979.

(19) Reich, M.; Deditius, A. P.; Chryssoulis, S.; Li, J. W.; Ma, C. Q.; Parada, M. A.; Barra, F.; Mittermayr, F. Pyrite as a record of hydrothermal fluid evolution in a porphyry copper system: A SIMS/EMPA trace element study. *Geochim. Cosmochim. Acta* **2013,** *104*, 42–62.

(20) Large, R. R.; Halpin, J. A.; Danyushevsky, L. V.; Maslennikov, V. V.; Bull, S. W.; Long, J. A.; Gregory, D. D.; Lounejeva, E.; Lyons, T. W.; Sack, P. J., et al. Trace element content of sedimentary pyrite as a new proxy for deep-time ocean-atmosphere evolution. *Earth Planet Sc. Lett.* **2014,** *389*, 209-220.

(21) Gregory, D. D.; Large, R. R.; Halpin, J. A.; Baturina, E. L.; Lyons, T. W.; Wu, S.; Danyushevsky, L.; Sack, P. J.; Chappaz, A.; Maslennikov, V. V., et al. Trace element content of sedimentary pyrite in black shales. *Econ. Geol.* **2015,** *110*, 1389–1410.

(22) Foster, A. L.; Brown, G. E.; Tingle, T. N.; Parks, G. A. Quantitative arsenic speciation in mine tailings using X-ray absorption spectroscopy. *Am. Miner.* **1998,** *83*, 553-568.

(23) Juillot, F.; Ildefonse, P.; Morin, G.; Calas, G.; deKersabiec, A. M.; Benedetti, M. Remobilization of arsenic from buried wastes at an industrial site: mineralogical and geochemical control. *Appl Geochem* **1999,** *14*, 1031-1048.

(24) Diehl, S. F.; Goldhaber, M. B.; Hatch, J. R. Modes of occurrence of mercury and other trace elements in coals from the warrior field, Black Warrior Basin, Northwestern Alabama. *Intern. J. Coal Geol.* **2004,** *59*, 193-208.

(25) Majzlan, J.; Lalinska, B.; Chovan, M.; Jurkovic, L.; Milovska, S.; Göttlicher, J. The formation, structure, and ageing of As-rich hydrous ferric oxide at the abandoned Sb deposit Pezinok (Slovakia). *Geochim. Cosmochim. Acta.* **2007,** *71*, 4206-4220.

(26) Tian, H.; Liu, K.; Zhou, J.; Lu, L.; Hao, J.; Qiu, P.; Gao, J.; Zhu, C.; Wang, K.; Hua, S. Atmospheric emission inventory of hazardous trace elements from China's coal-fired power plants - Temporal trends and spatial variation characteristics. *Environ. Sci. Technol.* **2014,** *48*, 3575-3582.

(27) Ellwood, M. J.; Schneider, L.; Potts, J.; Batley, G. E.; Floyd, J.; Maher, W. A. Volatile selenium fluxes from selenium-contaminated sediments in an Australian coastal lake. *Environ. Chem.* **2016,** *13*, 68–75.

(28) Li, J. W.; Chen, N.; Rajan, I.; Sun, Z.; Wu, H. M.; Chen, D.; Kong, L. The geochemical release feature of Tl in Tl-rich pyrite mine wastes: a long-term leaching test. *Environ. Sci. Pollut. Res.* **2017,** *24*, 12212-12219.

(29) D'Orazio, M.; Biagioni, C.; Dini, A.; Vezzoni, S. Thallium-rich pyrite ores from the Apuan Alps, Tuscany, Italy: constraints for their origin and environmental concerns. *Miner. Deposita* **2017,** *52*, 687-707.

(30) Khamkhash, A.; Srivastava, V.; Ghosh, T.; Akdogan, G.; Ganguli, R.; Aggarwal, S. Mining-related selenium contamination in Alaska, and the state of current knowledge. *Minerals* **2017,** *7*, n° 46.

(31) Lopez-Arce, P.; Garcia-Guinea, J.; Garrido, F. Chemistry and phase evolution during roasting of toxic thallium-bearing pyrite. *Chemosphere* **2017,** *181*, 447-460.

(32) Manceau, A.; Merkulova, M.; Murdzek, M.; Batanova, V.; Baran, R.; Glatzel, P.; Saikia, B. K.; Paktunc, D.; Lefticariu, L. Chemical forms of mercury in pyrite: Implications for predicting mercury releases in acid mine drainage settings. *Environ. Sci. Technol.* **2018,** *52*, 10286-10296.

(33) George, L. L.; Biagionia, C.; Leporeb, G. O.; Lacalamita, M.; Agrosìc, G.; Capitanid, G. C.; Bonaccorsia, E.; d'Acapito, F. The speciation of thallium in (Tl,Sb,As)-rich pyrite. *Ore Geol. Rev.* **2019,** *107*, 364-380.

(34) Simon, G.; Huang, H.; Penner-Hahn, J. E.; Kesler, S. E.; Kao, L. S. Oxidation state of gold and arsenic in gold-bearing arsenian pyrite. *Am. Mineral.* **1999,** *84*, 1071-1079.

(35) Paktunc, D. Speciation of arsenic in pyrite by micro-X-ray absorption fine-structure spectroscopy (XAFS). *Ninth International Congress for Applied Mineralogy* **2008,** *Brisbane, QLD, 8 - 10 September 2008*.

(36) Savage, K. S.; Tingle, T. N.; O'Day, P. A.; Waychunas, G. A.; Bird, D. K. Arsenic speciation in pyrite and secondary weathering phases, Mother Lode Gold District, Tuolumne County, California. *Appl. Geochem.* **2000,** *15*, 1219-1244.

(37) Lowers, H. A.; Breit, G. N.; Foster, A. L.; Whitney, J.; Yount, J. Arsenic incorporation into authigenic pyrite , Bengal Basin sediment , Bangladesh. *Geochim. Cosmochim. Acta.* **2007,** *71*, 2699–2717.

(38) Le Pape, P.; Blanchard, M.; Brest, J.; Boulliard, J. C.; Ikogou, M.; Stetten, L.; Wang, S.; Landrot, G.; Morin, G. Arsenic incorporation in pyrite at ambient temperature at both tetrahedral S^{-I} and octahedral Fe^{-II} sites: Evidence from EXAFS-DFT analysis. *Environ. Sci. Technol.* **2017,** *51*, 150-158.

(39) Blanchard, M.; Alfredsson, M.; Brodholt, J.; Wright, K.; Catlow, C. R. A. Arsenic incorporation into FeS_2 pyrite and its influence on dissolution: A DFT study. *Geochim. Cosmochim. Acta.* **2007,** *71*, 624-630.

(40) Reich, M.; Becker, U. First-principles calculations of the thermodynamic mixing properties of arsenic incorporation into pyrite and marcasite. *Chem Geol* **2006,** *225*, 278-290.

(41) Yakovleva, V. A.; Belogub, E. V.; Novoselov, K. A. Supergene iron sulpho-selenides from the Zapadno-Ozernoe copper-zinc massive sulphide deposit, South Urals, Russia: a new solid-solution series between pyrite FeS_2 and dzharkenite $FeSe_2$. *Min. Mag.* **2003,** *67*, 355-361.

(42) Batanova, V. G.; Sobolev, A. V.; Magnin, V. Trace element analysis by EPMA in geosciences: detection limit, precision and accuracy. *IOP Conf. Ser. Mater. Sci. Eng.* **2018,** *304*, 012001.

(43) Glatzel, P.; Sikora, M.; Smolentsev, G.; Fernandez-Garcia, M. Hard X-ray photon-in photon-out spectroscopy. *Catal. Today* **2009,** *145*, 294-299.

(44) Mathon, O.; Beteva, A.; Borrel, J.; Bugnazet, D.; Gatla, S.; Hino, R.; Kantor, I.; Mairs, T.; Munoz, M.; Pasternak, S., et al. The time-resolved and extreme conditions XAS (Texas) facility at the European Synchrotron Radiation Facility: The general-purpose EXAFS bending-magnet beamline BM23. *J. Synchrotron Radiat.* **2015,** *22*, 1548–1554.

(45) Manceau, A.; Marcus, M. A.; Tamura, N. Quantitative speciation of heavy metals in soils and sediments by synchrotron X-ray techniques. In *Applications of Synchrotron Radiation in Low-*

Temperature Geochemistry and Environmental Science, Fenter, P. A.; Rivers, M. L.; Sturchio, N. C.; Sutton, S. R., Eds. Mineralogical Society of America: Washington, DC, 2002; Vol. 49, pp 341-428.

(46) Dovesi, R.; Orlando, R.; Erba, A.; Zicovich-Wilson, C. M.; Civalleri, B.; Casassa, S.; Maschio, L.; Ferrabone, M.; De La Pierre, M.; D'Arco, P., et al. CRYSTAL14: A Program for the Ab initio investigation of crystalline solids. *Intern. J. Quant. Chem.* **2014,** *114*, 1287-1317.

(47) Smith, F. N.; Taylor, C. D.; Um, W.; Kruger, A. A. Technetium incorporation into goethite (α-FeOOH): An atomic-scale investigation. *Environ. Sci. Technol.* **2015,** *49*, 13699-13707.

(48) Smith, F. N.; Um, W.; Taylor, C. D.; Kim, D. S.; Schweiger, M. J.; Kruger, A. A. Computational investigation of technetium(IV) incorporation into inverse spinels: Magnetite (Fe_3O_4) and trevorite ($NiFe_2O_4$). *Environ. Sci. Technol.* **2016,** *50*, 5216-5224.

(49) Perdew, J. P.; Chevary, J. A.; Vosko, S. H.; Jackson, K. A.; Pederson, M. R.; Singh, D. J.; Fiolhais, C. Atoms, molecules, solids, and surfaces: applications of the generalized gradient approximation for exchange and correlation. *Phys. Rev. B* **1992,** *46*, 6671–6687.

(50) Perdew, J. P.; Ruzsinszky, A.; Csonka, G. I.; Vydrov, O. A.; Scuseria, G. E.; Constantin, L. A.; Zhou, X. L.; Burke, K. Restoring the density-gradient expansion for exchange in solids and surfaces. *Phys. Rev. Lett.* **2008,** *100*, 136406.

(51) Lichanot, A.; Apra, E.; Dovesi, R. Quantum-mechanical Hartree-Fock study of the elastic properties of Li_2S and Na_2S. *Phys. Status Solidi B* **1993,** *177*, 157-163.

(52) Heifets, E.; Kotomin, E. A.; Bagaturyants, A. A.; Maier, J. Thermodynamic stability of stoichiometric $LaFeO_3$ and $BiFeO_3$: a hybrid DFT study. *Phys. Chem. Chem. Phys.* **2017,** *19*, 3738-3755.

(53) Peintinger, M. F.; Oliveira, D. V.; Bredow, T. Consistent gaussian basis sets of triple-zeta valence with polarization quality for solid-state calculations. *J. Comput. Chem.* **2013,** *34*, 451-459.

(54) Heyd, J.; Peralta, J. E.; Scuseria, G. E.; Martin, R. L. Energy band gaps and lattice parameters evaluated with the Heyd-Scuseria-Ernzerhof screened hybrid functional. *J. Chem. Phys.* **2005,** *123*, 174101.

(55) Bindi, L.; Moelo, Y.; Leone, P.; Suchaud, M. Stoichiometric arsenopyrite, FeAsS, from La Roche-Balue quarry, Loire-Atlantique, France: Crystal structure and Mössbauer study. *Can. Miner.* **2012,** *50*, 471-479.

(56) Ondrus, P.; Vavrin, I.; Skala, R.; Veselovsky, F. Low-temperature Ni-rich löllingite from Haje, Pibram, Czech Republic. Rietveld crystal structure refinement. *Neues Jahr. Mineral. Abh.* **2001**, 169-185.

(57) Mandarino, J. A. New minerals recently approved by the commission on new minerals and mineral names, International Mineralogical Association. *Eur. J. Miner.* **1995,** *7*, 447-456.

(58) Peintinger, M. F.; Kratz, M. J.; Bredow, T. Quantum-chemical study of stable, meta-stable and high-pressure alumina polymorphs and aluminum hydroxides. *J. Mater. Chem. A* **2014,** *2*, 13143-13158.

(59) Ghazisaeed, S.; Majzlan, J.; Plasil, J.; Kiefer, B. A simple method for the prediction of the orientation of H_2O molecules in ionic crystals. *J. Appl. Crsyt.* **2018,** *51*, 1116-1124.

(60) Garrett, K. E.; Ritzmann, A. M.; Smith, F. N.; Kessler, S. H.; Devanathan, R.; Henson, N. J.; Abrecht, D. G. First principles investigation of the structural and bonding properties of hydrated actinide (IV) oxalates, $An(C_2O_4)_2.6H_2O$ (An = U, Pu). *Comp. Mater. Sci.* **2018,** *153*, 146-152.

(61) Monkhorst, H. J.; Pack, J. D. Special points for Brillouin-zone integrations. *Phys. Rev. B* **1976,** *13*, 5188–5192.

(62) Merkulova, M.; Murdzek, M.; Mathon, O.; Glatzel, P.; Batanova, V.; Manceau, A. Evidence for syngenetic micro-inclusions of As^{3+}- and As^{5+}-containing Cu sulfides in hydrothermal pyrite. *Am. Miner.* **2019,** *104*, 300-306.

(63) Joly, Y. X-ray absorption near-edge structure calculations beyond the muffin-tin approximation. *Phys. Rev. B* **2001,** *63*, n° 125120.

(64) Ankudinov, A. L.; Rehr, J. J. Relativistic calculations of spin-dependent X-ray-absorption spectra. *Phys. Rev. B* **1997,** *56*, 1712-1716.

(65) Bunau, O.; Joly, Y. Self-consistent aspects of x-ray absorption calculations. *J. Phys. Condens. Matter.* **2009,** *21*, 345501.

(66) Komnitsas, K.; Xenidis, A.; Adam, K. Oxidation of pyrite and arsenopyrite in sulphidic spoils in Lavrion. *Miner. Eng.* **1995,** *8*, 1443-1454.

FIGURE CAPTIONS

Figure 1. Polyhedral structure and bonding environment of sulfur in pyrite (a) and arsenopyrite (b). Pyrite has a cubic structure consisting of corner-sharing FeS_6 octahedra.[2] Arsenopyrite has a monoclinic structure consisting of single chains of edge-sharing $Fe(As_3S_3)$ octahedra cross-linked by sharing corners.[55] In pyrite, sulfur is bonded to one S atom at 2.16 Å (S_2^{2-} dianion) and to three Fe atoms at 2.26 Å ($[SFe]_1$ pair). The second sulfur shell ($[SS]_2$ pair) is split in two subshells at 3.08 Å

(short edges in orange) and 3.32 Å (long edges in green). In arsenopyrite, the As atoms form $[As]_3$ triads on octahedral faces.

Figure 2. Backscattered electron images of pyrite from Bolivia (a), Utah (b), Spain (c), Germany (d), and Switzerland (e), and distributions of As and Se in pyrite Ut, Sp, Ger, and Sw measured by EPMA. The red rectangles indicate the location in the grains of the SXRF maps. Map size: 300 × 80 pixels; pixel size: 2 × 2 μm^2; probe diameter: 2 μm; dwell time 500 ms; electron voltage = 20 kV, current = 500 nA. The pyrite from Bolivia is zoned. The brighter zones in pyrite Sp are chalcopyrite ($CuFeS_2$) inclusions.

Figure 3. As (a) and Se (b) HR-XANES spectra of pyrite. As (c) and Se (d) HR-XANES of reference compounds.

Figure 4. Experimental (a-c) and calculated (d-f) HR-XANES spectra of pyrite measured at the As (a,d) and Se (b,c,e,f) K-edge.

Figure 5. EXAFS spectra of pyrite measured at the As and Se K-edge (a), and pyrite and arsenopyrite measured at the As K-edge (b).

Figure 6. As K-edge EXAFS spectra (a-c) and Fourier transform magnitudes (f-h) of pyrite with model-fits. (d,e) Overlay plots of the fit residuals for models 1 and 2 (d) and models 1 and 3. The peak positions of the Fourier transforms are not corrected for phase shift, and consequently are shifted by ΔR ~ -0.3 to -0.4 Å relative to structural R distances. *Res* is the fit residual as the goodness-of-fit parameter: $Res = [\Sigma\{|\chi_{exp} - \chi_{fit}|\}/\Sigma\{|\chi_{exp}|\}] \times 100$.

Figure 7. Se K-edge EXAFS spectra (a-c) and Fourier transform magnitudes (f-h) of pyrite with model-fits. (d,e) Overlay plots of the fit residuals for models 1 and 2 (d) and models 1 and 3.

Figure 8. Bonding environment of As in the $Fe_{32}As_2S_{62}$ (a) and $Fe_{48}As_3S_{93}$ (b) equilibrium structures. The S-S edges in yellow are 3.08 Å long and the S-S edges in green are 3.32 Å long in unsubstituted pyrite (Figure 1a). The red line connects the dianionic pair. Distances are in angstrom.

Table 1. List of samples, and As and Se point and bulk concentrations measured by EPMA and ICP-ES/MS

Code name	Origin	Geological setting	[As] EPMA	[As] ICP-ES	[Se] EPMA	[Se] ICP-MS
Bol	Bolivia, MNHN[a] collection, Paris	Hydrothermal vein	0.15-1.14 wt.%	na[b]	b.d.l. – 70 ppm	na
Sw	St Gotthard tunnel, Switzerland	Hydrothermal vein	b.d.l.[c] - 60 ppm (*n*=5)	na	b.d.l.[d]	na
Ut	Park City, Utah, USA	Hydrothermal: epithermal	50-160 ppm (*n*=3)	250 ppm	318-428 ppm (*n*=3)	500 ppm
Sp	Alzo, Gipuzkoa, Spain	Sedimentary	b.d.l.[c] - 30 ppm (n=2)	na	b.d.l.	na
Ger	Neumark, Saxony, Germany	Sedimentary - skarn	na	1590 ppm	na	80 ppm

[a]Museum National d'Histoire Naturelle; [b]Not analyzed; [c]Below detection limit (23 ppm); [d]Below detection limit (34 ppm).

Table 2. EXAFS parameters and interatomic distances in pyrite relative to a central S atom

Pyrite[a]			As Pyrite Bol – Model 1				As Pyrite Bol – Model 2				Se Pyrite Ut – Model 1				Se Pyrite Ut – Model 2			
Atom	*CN*[b]	*R*, Å[c]	Atom	*CN*	*R*, Å	σ[d], Å^2	Atom	*CN*	*R*, Å	σ, Å^2	Atom	*CN*	*R*, Å	σ, Å^2	Atom	*CN*	*R*, Å	σ, Å^2
S	1	2.16	S	1[e]	2.27	0.0031[f]	S	1[e]	2.27	0.0031[f]	S	1[e]	2.24	0.0024[f]	S	1[e]	2.24	0.0024[f]
Fe	3	2.26	Fe	3[e]	2.33	0.0031[f]	Fe	3[e]	2.33	0.0031[f]	Fe	3[e]	2.32	0.0024[f]	Fe	3[e]	2.32	0.0024[f]
S	6	3.08	S	5.9[g]	3.08	0.0056[f]	S	6.3[g]	3.16	0.0058[f]	S	6.5[g]	3.09	0.0040[f]	S	6.6[g]	3.15	0.0038[f]
S	6	3.32	S	6.1[g]	3.33	0.0056[f]	As	5.7[g]	3.16	0.0058[f]	S	5.5[g]	3.33	0.0040[f]	Se	4.4[g]	3.16	0.0038[f]
Fe	3	3.45	Fe	3[e]	3.52	0.0056[f]	Fe	3[e]	3.52	0.0058[f]	Fe	3[e]	3.52	0.0040[f]	Fe	3[e]	3.52	0.0038[f]
			ΔE[h] = 7.0 eV, *Res*[i] = 3.1				ΔE = 7.2 eV, *Res* = 3.4				ΔE = 5.7 eV, *Res* = 3.8				ΔE = 5.3 eV, *Res* = 4.4			

[a]After Rieder et al. [2]; [b]Coordination number; [c]Interatomic distance; [d]Debye-Waller factor; [e]Fixed value; [f]Parameters constrained identical; [g]Sum fixed to twelve; [h]Shift of energy threshold; [i]Fit residual. *Res* = $[\Sigma\{|\chi_{exp} - \chi_{fit}|\}/\Sigma\{|\chi_{exp}|\}] \times 100$.

Table 3. Difference of energy between the dilute and the cluster models for the $FeSe_xS_{2-x}$ and $FeAs_xS_{2-x}$ supercells[a]

Model	Supercell dimension	Number of Se/As atoms	[Se/As] weight %	Description	kcal/mol	eV/cell
2Se-1	222	2	4.0	Two Se atoms at long distance	0.00	0.000
2Se-2	222	2	4.0	One [SeSe]1 pair	-6.52	-0.035
2Se-3	222	2	4.0	One [SeSe]2 pair on long edge	0.01	0.000
2Se-4	222	2	4.0	One [SeSe]2 pair on short edge	-0.19	-0.001
3Se-1	322	3	4.0	Three Se atoms at long distance	0.00	0.000
3Se-2	322	3	4.0	One [SeSe]1 pair + one [SeSe]2 pair on short edge	-6.75	-0.024
3Se-3	322	3	4.0	Three [SeSe]2 pairs on a face with three long edges	-0.04	0.000
3Se-4	322	3	4.0	Three [SeSe]2 pairs on a face with two short and one long edge	-0.43	-0.002
2As-1	222	2	3.8	Two As atoms at long distance	0.00	0.000
2As-2	222	2	3.8	One [AsAs]1 pair	-21.25	-0.115
2As-3	222	2	3.8	One [AsAs]2 pair on long edge	4.73	0.026
2As-4	222	2	3.8	One [AsAs]2 pair on short edge	4.54	0.025
3As-1	322	3	3.8	Three As atoms at long distance	0.00	0.000
3As-2	322	3	3.8	One [AsAs]1 pair + one [AsAs]2 pair on short edge	-8.84	-0.032
3As-3	322	3	3.8	One isolated As + one [AsAs]2 pair on long edge	5.65	0.020
3As-4	322	3	3.8	Two [AsAs]2 pairs on short edges	6.64	0.024
3As-5	322	3	3.8	Two [AsAs]2 pairs on long edges	7.90	0.029
3As-6	322	3	3.8	Two [AsAs]2 pairs, one on short and another on long edge	8.84	0.032
3As-7	322	3	3.8	Three [AsAs]2 pairs on a face with three long edges	11.48	0.041
3As-8	322	3	3.8	Three [AsAs]2 pairs on a face with two short and one long edge	12.92	0.047

[a]A negative difference of E(dilute) – E(cluster) is unfavorable.

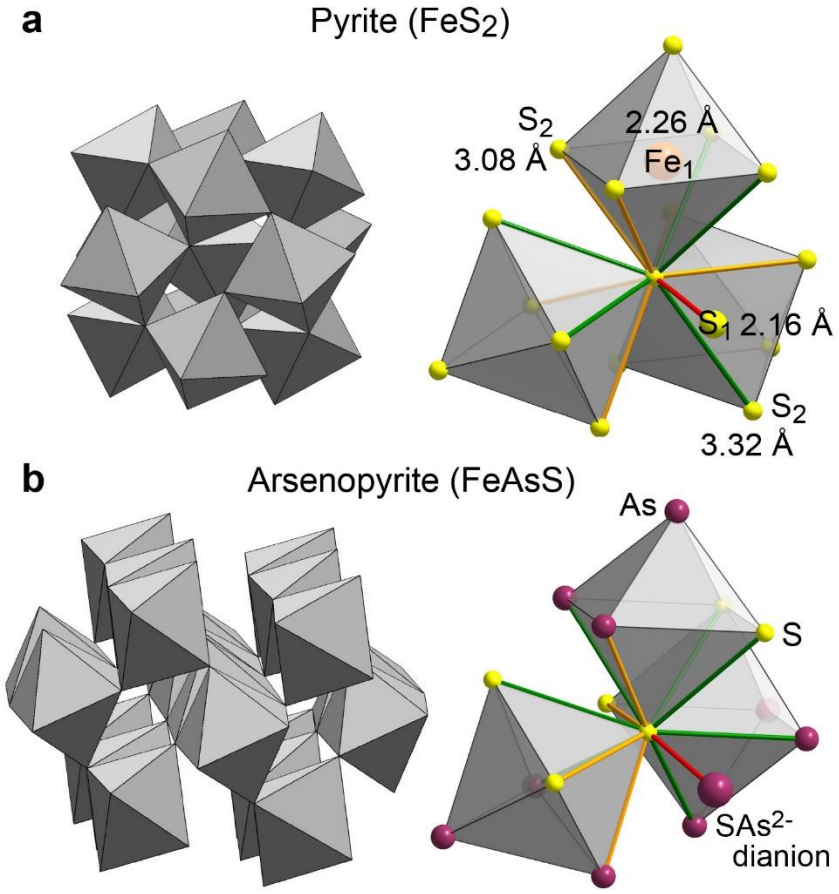
a
Pyrite (FeS_2)
S_2
3.08 Å
2.26 Å
Fe_1
S_1 2.16 Å
S_2
3.32 Å
b
Arsenopyrite (FeAsS)
As
S
SAs^{2-}
dianion

Figure 1

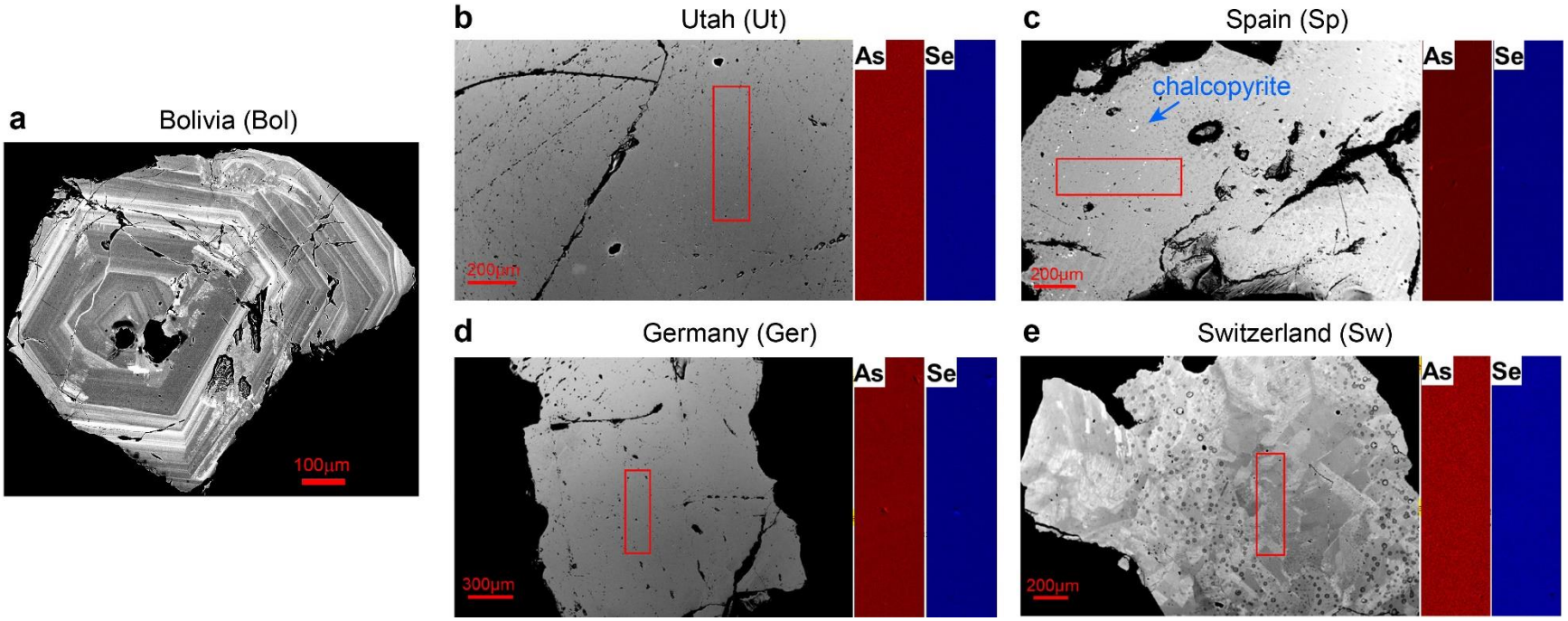
a
Bolivia (Bol)
100µm
b
Utah (Ut)
200µm
As
Se
c
Spain (Sp)
chalcopyrite
200µm
As
Se
d
Germany (Ger)
300µm
As
Se
e
Switzerland (Sw)
200µm
As
Se

Figure 2

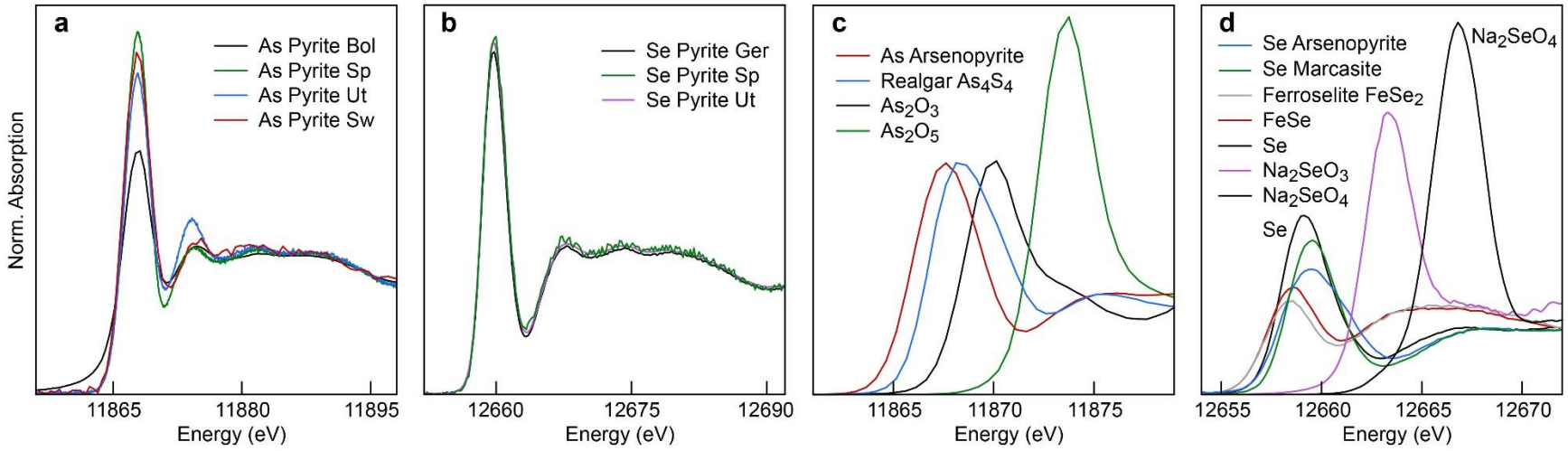
a
As Pyrite Bol
As Pyrite Sp
As Pyrite Ut
As Pyrite Sw
Norm. Absorption
11865
11880
11895
Energy (eV)
b
Se Pyrite Ger
Se Pyrite Sp
Se Pyrite Ut
12660
12675
12690
Energy (eV)
c
As Arsenopyrite
Realgar As_4S_4
As_2O_3
As_2O_5
11865
11870
11875
Energy (eV)
d
Se Arsenopyrite
Se Marcasite
Ferroselite $FeSe_2$
FeSe
Se
Na_2SeO_3
Na_2SeO_4
Na_2SeO_4
Se
12655
12660
12665
12670
Energy (eV)

Figure 3

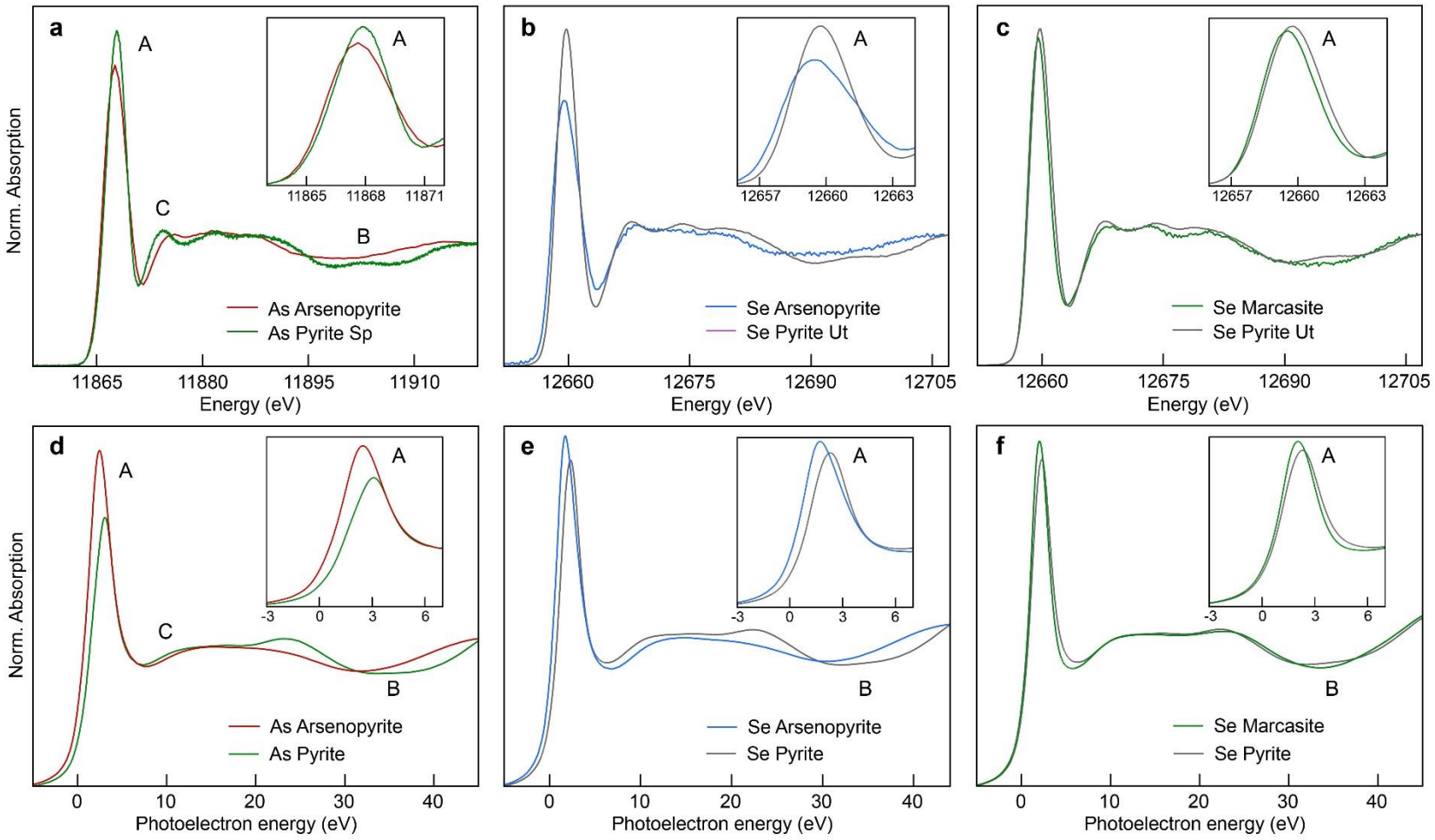
a
A
C
B
As Arsenopyrite
As Pyrite Sp
Norm. Absorption
Energy (eV)
b
Se Arsenopyrite
Se Pyrite Ut
c
Se Marcasite
Se Pyrite Ut
d
As Arsenopyrite
As Pyrite
Photoelectron energy (eV)
e
Se Arsenopyrite
Se Pyrite
f
Se Marcasite
Se Pyrite

Figure 4

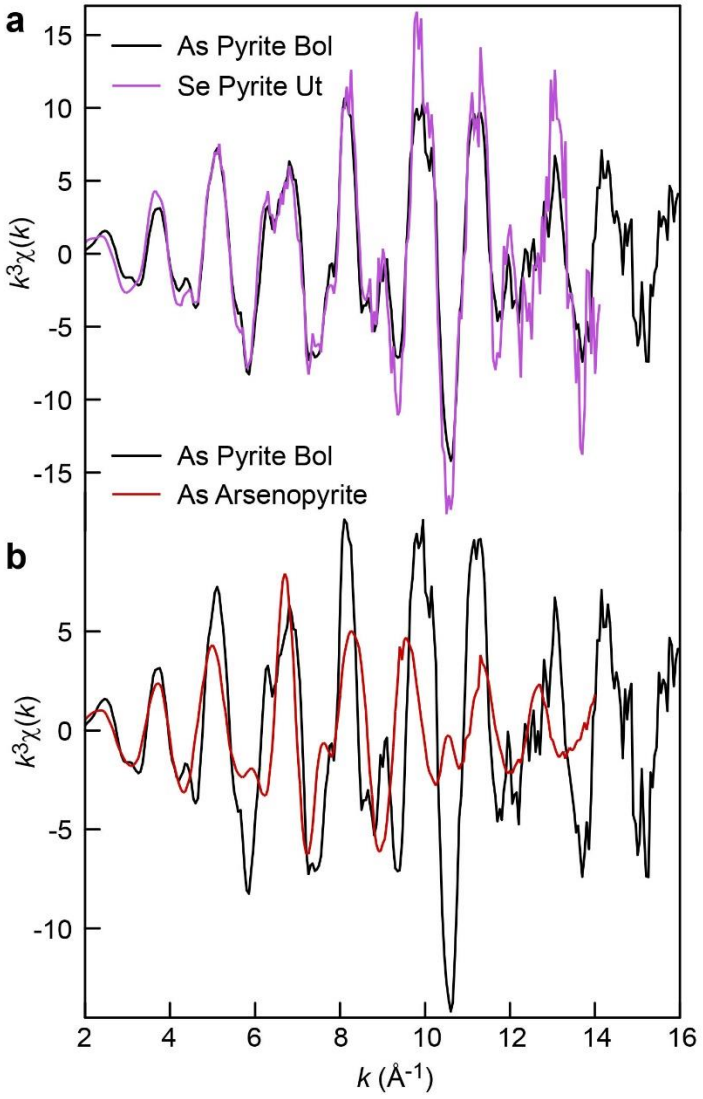
a
As Pyrite Bol
Se Pyrite Ut
$k^3\chi(k)$
15
10
5
0
-5
-10
-15
As Pyrite Bol
As Arsenopyrite
b
5
0
-5
-10
2
4
6
8
10
12
14
16
k (Å^{-1})

Figure 5

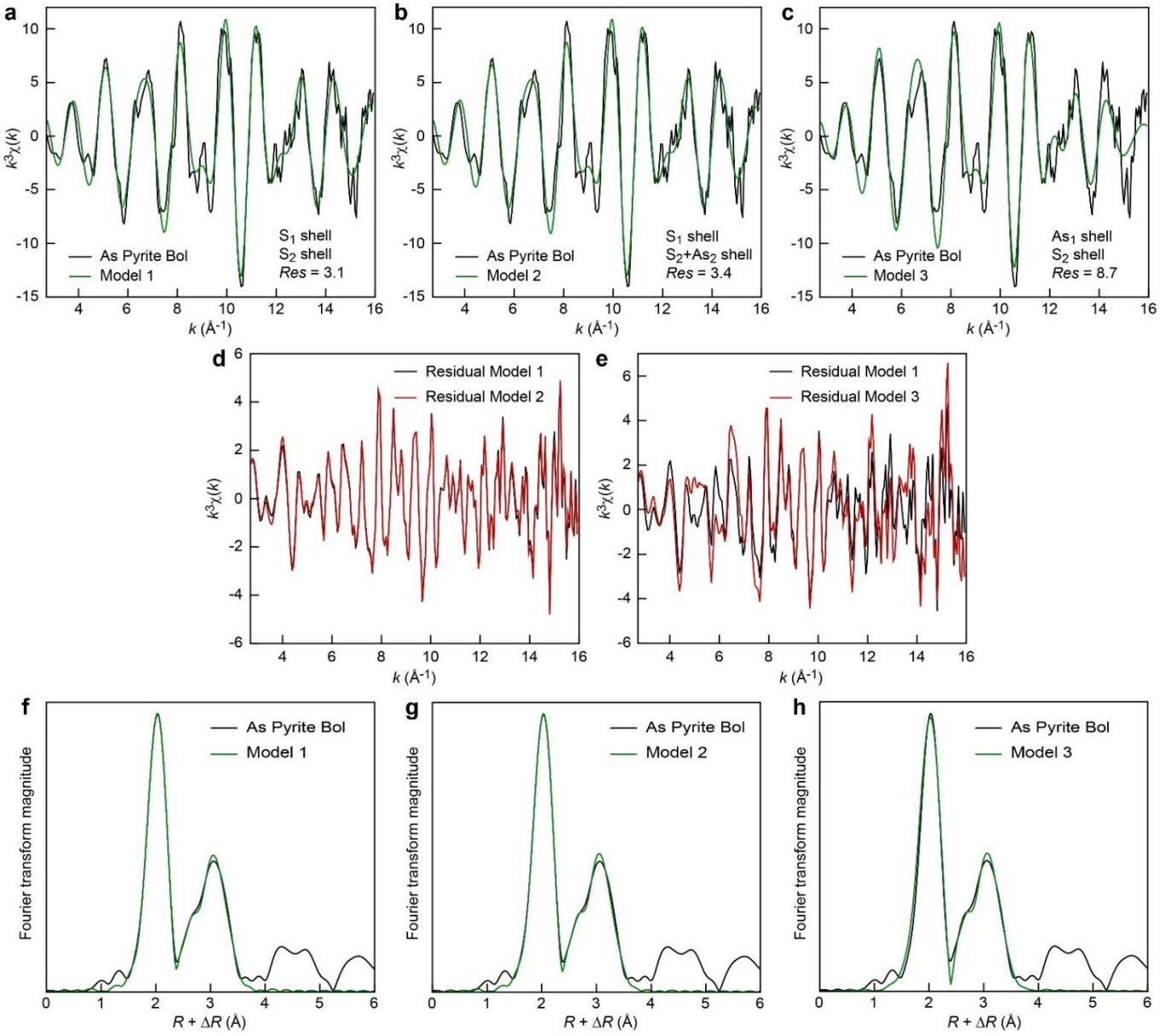
a
b
c
d
e
f
g
h
As Pyrite Bol
Model 1
Model 2
Model 3
S1 shell
S2 shell
Res = 3.1
S1 shell
S2+As2 shell
Res = 3.4
As1 shell
S2 shell
Res = 8.7
Residual Model 1
Residual Model 2
Residual Model 3
k (Å-1)
k3χ(k)
Fourier transform magnitude
R + ΔR (Å)

Figure 6

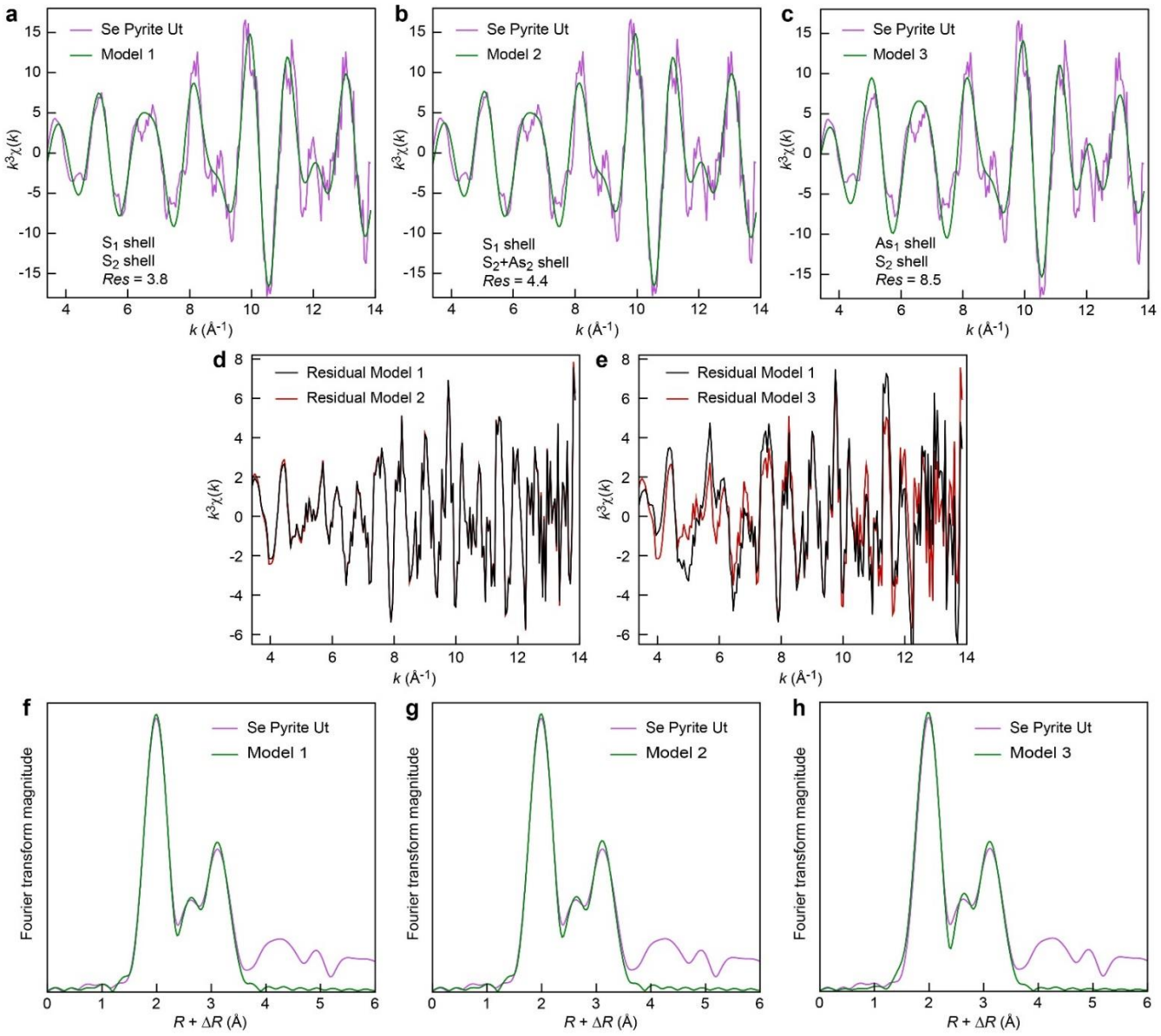
a
Se Pyrite Ut
Model 1
S1 shell
S2 shell
Res = 3.8
b
Se Pyrite Ut
Model 2
S1 shell
S2+As2 shell
Res = 4.4
c
Se Pyrite Ut
Model 3
As1 shell
S2 shell
Res = 8.5
d
Residual Model 1
Residual Model 2
e
Residual Model 1
Residual Model 3
f
Se Pyrite Ut
Model 1
g
Se Pyrite Ut
Model 2
h
Se Pyrite Ut
Model 3
k3χ(k)
k (Å-1)
Fourier transform magnitude
R + ΔR (Å)

Figure 7

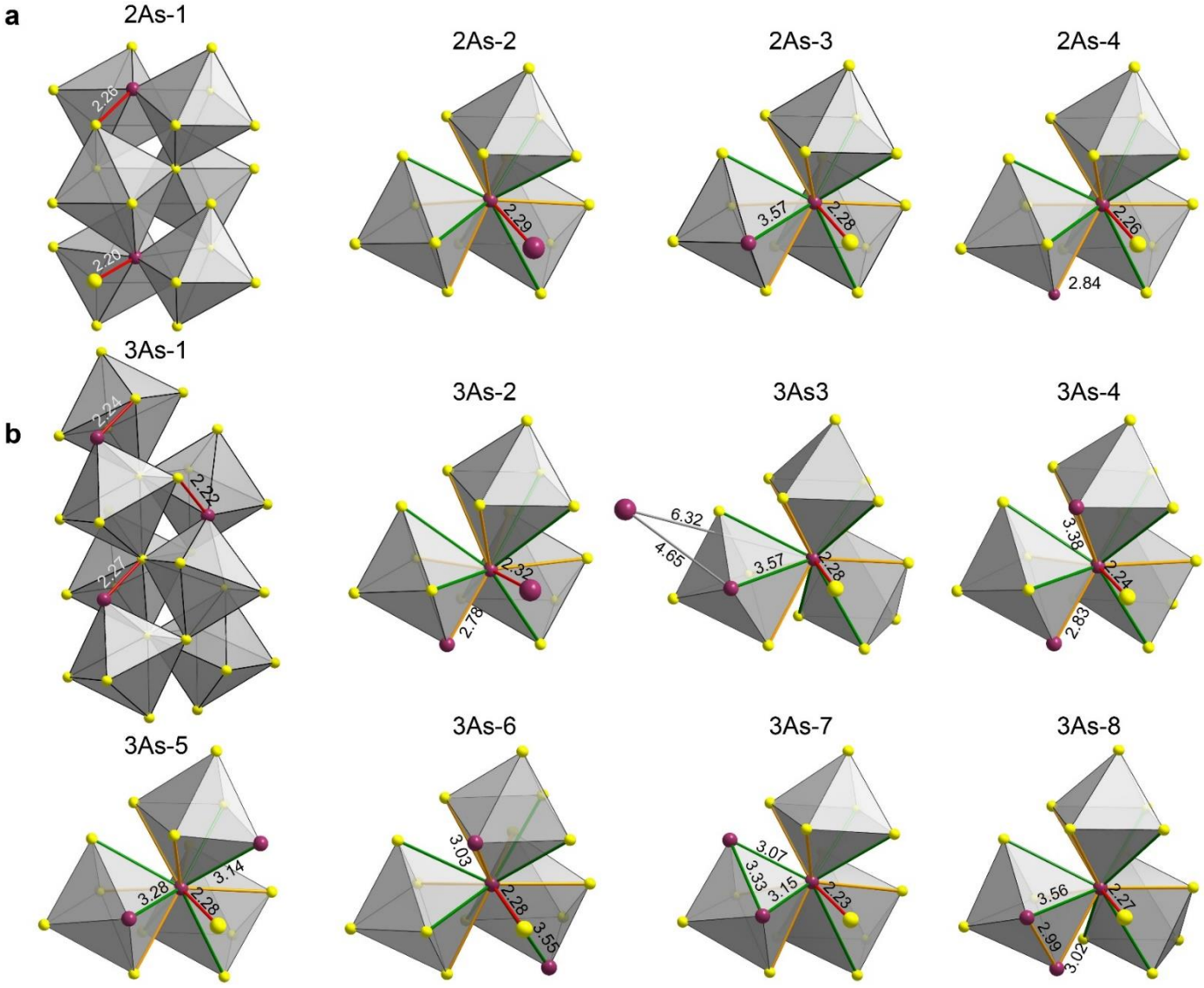
a
2As-1
2.26
2.20
2As-2
2.29
2As-3
3.57
2.28
2As-4
2.26
2.84
b
3As-1
2.24
2.22
2.27
3As-2
2.32
2.78
3As3
6.32
4.65
3.57
2.28
3As-4
3.38
2.24
2.83
3As-5
3.14
3.28
2.28
3As-6
3.03
2.28
3.55
3As-7
3.07
3.33
3.15
2.23
3As-8
3.56
2.27
2.99
3.02

Figure 8

Supplementary information for the article

The mode of incorporation of As(-I) and Se(-I) in natural pyrite revisited

Alain Manceau[*1], Margarita Merkulova*[*2], Olivier Mathon[2], Pieter Glatzel[2], Magdalena Murdzek[2], Valentina Batanova[1], Alexandre Simionovici[1], Stephan N. Steinmann[3], Dogan Paktunc[4]*

[1]Univ. Grenoble Alpes, CNRS, ISTerre, CS 40700, 38058 Grenoble, France

[2]European Synchrotron Radiation Facility (ESRF), 71 Rue des Martyrs, 38000 Grenoble, France

[3]Univ. Lyon, ENS de Lyon, CNRS, Laboratoire de Chimie, 69342 Lyon, France

[4]Nat. Resources Canada, CanmetMINING, 555 Booth St, Ottawa, ON, Canada

Content

1. Materials and methods

1.1. Sample preparation

Fragments of pyrite crystals were embedded in epoxy resin and polished for EPMA, SXRF mapping, and micro EXAFS measurement. Other fragments were crushed in an agate mortar inside a glove bag filled with He to prevent oxidation. Powder was stored in a desiccator and pressed into 5-mm diameter pellets for bulk HR-XANES and EXAFS measurements.

1.2. XRD

The X-ray powder diffraction patterns for the five pyrite samples were measured at ISTerre (Grenoble, France) in reflection geometry using a BrukerD8 diffractometer equipped with a selective energy SolXEM (Baltics Instruments) detector. Electron voltage and current were 40 kV and 40 mA. Intensity from the diffracted Cu $K\alpha_1$ line was measured from 5 to 90° 2θ with a step size of 0.03° and a dwell time of 6 s per step. The XRD traces are shown in Figure S2a. No mineral impurity was detected.

Arsenic and selenium references were mounted in a glass capillary of 1 mm diameter and characterized in transmission geometry with a Göbel optics. The dwell time was 6 s per step of 0.024°. The XRD traces are shown in Figures S2b and S2c. No mineral impurity was detected.

1.3. ICP-ES/MS

The concentrations of As and Se in bulk pyrite from Utah (Ut) and Germany (Ger) were measured by ICP-ES and ICP-MS, respectively, at Bureau Veritas (Canada). Analytical code AQ270 (ICP-ES/MS with digestion in aqua-regia) was used. Certified standard references and blanks were measured in the same conditions as pyrite. Results are given in Table 1. The percent error is 5% for As and 9% for Se.

1.4. EPMA

Backscattered electron (BSE) images, EPMA and elemental maps of pyrite were recorded with a JEOL JXA-8230 electron microprobe at ISTerre. As, Se, and Au were analyzed with a wavelength-dispersive spectrometer (WDS), and S and Fe with an energy-dispersive spectrometer (EDS). Operating conditions were 20 kV accelerating voltage and 900 nA beam current with a focused beam of 1-3 μm in diameter. The following certified natural and synthetic materials were used for standardization: As: InAs and FeAsS; Se: Se and Bi_2Se_3; Au: Au; Fe: $CuFeS_2$ and FeS_2; and S: $CuFeS_2$. The lowest and the highest As and Se contents are reported in Table 1. Elemental maps were acquired for As, Se , Au, Fe, and S (Figures S3 and S4a). Details on analytical precisions and determination of detection limits can be found in Batanova et al.[1]

1.5. Bulk HR-XANES

The As and Se K-edge HR-XANES spectra were collected on beamline ID26 of the ESRF. The storage ring was operated in the 7/8 + 1 filling mode, with 200 mA current. Rejection of higher harmonics and reduction of heat load were achieved with a white beam Pd-coated, flat mirror working under total reflection at 2.5 mrad deflecting angle. The energy of the incoming beam was selected with the 111 reflection of a Si double crystal monochromator, and the beam was focused horizontally by a second Pd-coated mirror and vertically by a third Pd-coated mirror. The flux on the sample was approximately 10^{13} photon/s in a beam footprint of ~700 (H) x 80 (V) μm^2 FWHM. The As $K\alpha_1$ fluorescence line was selected using the 555 reflection of five spherically bent (1 m radius) Si analyzer crystals (diameter = 100 mm) aligned at 69.85° Bragg angle in a vertical Rowland geometry. The Se $K\alpha_1$ fluorescence line was selected using the Si(844) reflection at a Bragg angle of 85.17°. The diffracted intensity was measured with an avalanche photodiode (APD). The effective energy resolution was 2.3 eV.

Spectra were measured at 10-15 K using a helium flow cryostat. Fifty scans of 20 s were acquired for the As and Se references and from 60 to 90 scans of 30 s for pyrite. The samples were moved horizontally and vertically after every scan to access unexposed material. No changes in spectral features were noted during the course of data collection that would indicate oxidation of pyrite or other radiation damage. Spectra were averaged with the PyMCA software[2] and reduced with the Labview suite of programs from beamline 10.3.2 at the Advanced Light Source (Berkley, USA).[3, 4] They were normalized to a unit step in the absorption coefficient at 11939 eV for As and at 12707 eV for Se.

1.6. Bulk and micro EXAFS

Bulk As and Se K-edge and micro As K-edge EXAFS spectra were collected at room temperature on beamline BM23 of the ESRF. The incoming beam was monochromated with a Si(111) double

crystal monochromator. The footprint on the sample of the unfocused beam was ~2.8 (H) x 0.5 (V) mm^2 FWHM. For micro EXAFS measurements, the monochromatic X-ray beam was focused to 5 x 5 μm^2 with a set of Pt-coated Kirkpatrick–Baez (KB) mirrors.[5] The flux incident on the sample was approximately 5 x 10^9 photons/sec. Micro EXAFS data were taken on points of interests chosen on a SXRF map measured at 14 keV, 5 µm step size, and 2 s/point measuring time (Figures S5 and S6). No beam damage was observed. EXAFS data were reduced with the Athena software[6] and fit with WinXAS.[7] Theoretical amplitude and phase shift functions were generated with FEFF7[8] using the arsenopyrite structure[9] for As and Se-substituted arsenopyrite for Se. The amplitude reduction factor (S_o^2) was fixed to 0.9. Fit results are given in Table 2.

1.7. Density Functional Theory (DFT)

Calculations were considered being converged when the total energy obtained in the self-consistent field (SFC) procedure differed by less than 10^{-7} a.u. (E_h) in two successive cycles (0.0027 meV). Default thresholds were used for the geometry optimizations. The two-electron integral tolerance setting 7 7 7 9 30 (TOLINTEG keyword) was preferred because of the recommendation of combined hybrid functionals and pseudopotentials.[10] Other settings were tested to verify that the SCF convergence was well achieved (Table S15, 6 6 6 6 12 is default). The shrinking factor IS also was tested (Tables S16 and S17). A factor of 6 was sufficient to converge the total energy with a precision of 10^{-7} a.u. The ANDERSON's method[11] and a FMIXING of 90% were used to accelerate the convergence. No symmetry restriction was applied during geometry optimization.

Basis sets and their abbreviations in Tables are:

Sulfur

Lichanot: all-electron split-valence 6-311G[12]
TZVP: triple-zeta valence with polarization[13]
Durand: effective Durand pseudopotential[14]

Iron:

Towler: all-electron split-valence 6-411d41G basis set[15]
TZVP: Triple-zeta valence with polarization[13]
ECP_Heifets: effective core pseudopotential[16, 17]
Durand: effective Durand pseudopotential[14]

Arsenic:

pp_Heyd: effective core pseudopotential, m-pVDZ double zeta quality with polarization functions[10]
TZVP: Triple-zeta valence with polarization[13]
Durand: effective Durand pseudopotential[14]
HWLC, val Durand: Hay-Wadt large-core pseudopotential[18] with valence electrons from Durand[14]
HWLC, val TZVP: Hay-Wadt large-core pseudopotential[18] with valence electrons from TZVP
HWLC, val Heyd: Hay-Wadt large-core pseudopotential[18] with valence electrons from pp_Heyd[10]

Selenium

pp_Heyd: effective core pseudopotential, m-pVDZ double zeta quality with polarization functions[10]
TZVP: Triple-zeta valence with polarization[13]

2. Supplementary tables

Table S1. Comparison between experimental and calculated ionization energies for S. Energy is in kcal/mol.

		S^{1+}		S^{2+}		S^{1-}		S^{2-}	
		Energy	Difference, %	Energy	Difference, %	Energy	Difference, %	Energy	Difference, %
Experiment		238.28	-	536.82	-	-4761	-	165.37	-
Basis set	Functional								
Lichanot	PBEsol0	277.13	*16.31*	508.01	*-5.37*	-74.78	*57.07*	102.03	*-38.30*
	PW1PW	276.48	*16.03*	509.90	*-5.01*	-71.74	*50.69*	106.84	*-35.40*
TZVP	PBEsol0	273.63	*14.84*	506.37	*-5.67*	-64.60	*35.68*	123.28	*-25.45*
	PW1PW	273.76	*14.89*	509.07	*-5.17*	-62.14	*30.51*	127.87	*-22.68*
Durand	PBEsol0	286.43	*20.21*	516.36	*-3.81*	-78.51	*64.90*	114.44	*-30.80*
	PW1PW	285.57	*19.85*	518.62	*-3.39*	-75.24	*58.04*	119.40	*-27.80*

Table S2. Comparison between experimental and calculated ionization energies for Fe. Energy is in kcal/mol.

		Fe^{1+}		Fe^{2+}		Fe^{3+}	
		Energy	Difference, %	Energy	Difference, %	Energy	Difference, %
Experiment		181.76	-	372.58	-	704.97	-
Basis set	Functional						
Towler	PBEsol0	98.08	*-46.03*	425.68	*14.25*	796.65	*13.00*
	PW1PW	92.65	*-49.03*	422.34	*13.35*	796.34	*12.96*
TZVP	PBEsol0	-	-	431.68	*15.86*	791.09	*12.22*
	PW1PW	-	-	428.67	*15.05*	790.75	*12.17*
ECP_Heifets	PBEsol0	124.94	*-31.26*	435.25	*16.82*	798.44	*13.26*
	PW1PW	-	-	432.36	*16.05*	798.60	*13.28*
Durand	PBEsol0	59.11	*-67.48*	424.65	*13.98*	830.09	*17.75*
	PW1PW	56.93	*-68.68*	425.49	*14.20*	835.08	*18.46*

Table S3. Comparison between experimental and calculated ionization energies for As. Energy is in kcal/mol.

		As^{1+}		As^{2+}		As^{3+}		As^{4+}		As^{5+}		As^{1-}	
		Energy	Difference, %	Energy	Difference, %	Energy	Difference, %	Energy	Difference, %	Energy	Difference, %	Energy	Difference, %
Experiment		225.14	-	427.55	-	652.03	-	1153.45	-	1443.71	-	-18.58	-
Basis set	Functional												
pp_Heyd	PBEsol0	202.00	*-10.28*	396.91	*-7.17*	608.25	*-6.71*	1164.90	*0.99*	1415.94	*-1.92*	-21.34	*14.86*
	PW1PW	202.20	*-10.19*	399.56	*-6.55*	613.82	*-5.86*	1164.67	*0.97*	1426.68	*-1.18*	-19.77	*6.39*
TZVP	PBEsol0	206.33	*-8.35*	396.73	*-7.21*	606.42	*-6.99*	1147.54	*-0.51*	1393.32	*-3.49*	-32.01	*72.26*
	PW1PW	206.45	*-8.30*	399.51	*-6.56*	611.98	*-6.14*	1147.32	*-0.53*	1404.77	*-2.70*	-30.51	*64.16*
Durand	PBEsol0	222.98	*-0.96*	426.41	*-0.26*	643.15	*-1.36*	1096.45	*-4.94*	-	-	-32.09	*72.65*
	PW1PW	224.98	*-0.07*	431.10	*0.83*	650.70	*-0.20*	1096.98	*-4.90*	-	-	-31.81	*71.19*
HWLC, val	PBEsol0	222.05	*-1.37*	384.76	*-10.01*	542.72	*-16.76*	1070.10	*-7.23*	-	-	-57.74	*210.72*
Heyd	PW1PW	223.62	*-0.67*	387.34	*-9.40*	546.53	*-16.18*	1070.81	*-7.16*	-	-	-58.07	*212.48*
HWLC, val	PBEsol0	62.89	*-72.07*	393.71	*-7.91*	602.00	*-7.67*	1119.48	*-2.95*	-	-	-168.58	*807.18*
TZVP	PW1PW	204.90	*-8.99*	398.43	*-6.81*	609.28	*-6.56*	1120.05	*-2.90*	-	-	-27.69	*48.99*
HWLC, val	PBEsol0	222.88	*-1.00*	424.60	*-0.69*	639.18	*-1.97*	1092.61	*-5.27*	-	-	-33.09	*78.04*
Durand	PW1PW	224.85	*-0.13*	429.19	*0.38*	646.61	*-0.83*	1093.05	*-5.24*	-	-	-32.84	*64.16*

Table S4. Comparison between experimental and calculated ionization energies for Se. Energy is in kcal/mol.

		Se^{1+}		Se^{2+}		Se^{3+}		Se^{4+}		Se^{5+}		Se^{6+}		Se^{1-}	
		Energy	Difference, %	Energy	Difference, %	Energy	Difference, %	Energy	Difference, %	Energy	Difference, %	Energy	Difference, %	Energy	Difference, %
Experiment		224.25	-	487.51	-	729.03	-	987.78	-	1570.90	-	1882.09	-	-46.57	
Basis set	Functional														
pp_Heyd	PBEsol0	255.19	*13.80*	462.56	*-5.12*	690.10	*-5.34*	935.06	*-5.34*	1575.63	*0.30*	1851.21	*-1.64*	-65.50	*40.64*
	PW1PW	253.65	*13.11*	463.47	*-4.93*	693.75	*-4.84*	941.59	*-4.68*	1575.70	*0.31*	1863.50	*-0.99*	-61.97	*33.07*
TZVP	PBEsol0	265.31	*18.31*	468.62	*-3.87*	697.47	*-4.33*	947.97	*-4.03*	1527.69	*-2.75*	1776.41	*-5.62*	-82.82	*77.84*
	PW1PW	263.52	*17.51*	469.96	*-3.60*	701.78	*-3.74*	954.54	*-3.36*	1527.76	*-2.75*	1788.87	*-4.95*	-79.34	*70.37*

Table S5. Results of basis set and functionals testing for pyrite single cell. First two combinations were chosen for As-pyrite and Se-pyrite calculations, respectively.

Pyrite FeS_2			
Basis sets	Functional	Lattice parameter *a*, Å	Difference, %
Experiment (Rieder et al., 2007)		5.416	-
S: Lichanot Fe: ECP_Heifets	PW1PW	5.518	*1.89*
S: Lichanot Fe: TZVP	PW1PW	5.471	*1.01*
S: Lichanot Fe: Towler	PBEsol0 PW1PW	5.418 5.480	*0.06* *1.17*
S: TZVP Fe: Towler	PBEsol0 PW1PW	5.330 5.393	*-1.58* *-0.42*
S: TZVP Fe: TZVP	PBEsol0 PW1PW	5.340 5.402	*-1.40* *-0.27*
S: TZVP Fe: ECP_Heifets	PBEsol0 PW1PW	5.363 5.437	*-0.97* *0.38*
S: Durand Fe: Durand	PBEsol0 PW1PW	5.674 5.767	*4.76* *6.47*

Table S6. Results of basis set and functionals testing for arsenopyrite single cell.

Arsenopyrite FeAsS									
		Lattice parameters						angle	
Basis sets	Functional	*a*, Å	Difference, %	*b*, Å	Difference, %	*c*, Å	Difference, %	β, °	Difference, %
Experiment (Bindi, 2012)		5.761	-	5.684	-	5.767	-	111.721	-
S: lichanot As: pp_Heyd Fe: ECP_Heifets	PBEsol0	5.642	*-2.07*	5.646	*-0.67*	5.667	*-1.73*	112.434	*0.64*
	PW1PW	5.714	*-0.82*	5.717	*0.58*	5.737	*-0.53*	112.308	*0.53*
S: lichanot As: TZVP Fe: ECP_Heifets	PBEsol0	5.637	*-2.15*	5.637	*-0.84*	5.660	*-1.86*	112.590	*0.78*
	PW1PW	5.706	*-0.96*	5.703	*0.34*	5.726	*-0.72*	112.421	*0.63*
S: lichanot As: TZVP Fe: Towler	PBEsol0	5.618	*-2.48*	5.610	*-1.31*	5.635	*-2.30*	112.595	*0.78*
	PW1PW	5.683	*-1.36*	5.669	*-0.27*	5.697	*-1.22*	112.455	*0.66*
S: lichanot As: pp_Heyd Fe: Towler	PBEsol0	5.619	*-2.47*	5.615	*-1.21*	5.643	*-2.15*	112.389	*0.60*
	PW1PW	5.684	*-1.33*	5.677	*-0.13*	5.707	*-1.05*	112.219	*0.45*
S: TZVP As: TZVP Fe: TZVP	PBEsol0	5.580	*-3.14*	5.587	*-1.71*	5.609	*-2.74*	112.377	*0.59*
	PW1PW	5.643	*-2.05*	5.644	*-0.70*	5.674	*-1.62*	112.215	*0.44*
S: Durand As: Durand Fe: Durand	PBEsol0	5.743	*-0.31*	5.808	*2.17*	5.734	*-0.57*	114.650	*2.62*
	PW1PW	5.912	*2.62*	6.003	*5.62*	5.951	*3.18*	116.137	*3.95*
S: Lichanot As: HWLC, val Durand Fe: Towler	PBEsol0	5.622	*-2.42*	5.611	*-1.29*	5.629	*-2.40*	112.698	*0.87*
	PW1PW	5.673	*-1.53*	5.662	*-0.39*	5.681	*-1.50*	112.540	*0.73*
S: Lichanot As: HWLC, val TZVP Fe: Towler	PBEsol0	5.632	*-2.24*	5.627	*-1.00*	5.651	*-2.02*	112.595	*0.78*
	PW1PW	5.687	*-1.29*	5.681	*-0.05*	5.706	*-1.06*	112.430	*0.63*

Table S7. Results of basis set and functionals testing for dzharkenite single cell.

Dzharkenite $FeSe_2$			
Basis sets	Functional	Lattice parameter *a*, Å	Difference, %
Experiment (Mandarino, 1995)		5.783	-
Se: pp_Heyd	PW1PW	5.792	*0.16*
Fe: TZVP	PBEsol0	5.721	*1.12*
Se: pp_Heyd Fe: ECP_Heifets	PW1PW	5.822	*0.63*
Se: pp_Heyd	PBEsol0	5.705	*1.40*
Fe: Towler	PW1PW	5.774	*0.21*

Table S8. Optimized versus experimental lattice parameter and interatomic distances of pyrite. PW1PW functional, Lichanot basis set for S and ECP_Heifets basis set for Fe were applied for calculations.

Parameter	Optimized structure	Rieder et al., 2007	difference, %
a, Å	5.518	5.416	*1.89*
S-S, Å	2.15	2.16	*-0.46*
Fe-S, Å	2.31	2.26	*2.21*
S-S, Å	3.15	3.08	*2.27*
S-S, Å	3.38	3.32	*1.81*

Table S9. Optimized versus experimental lattice parameter and interatomic distances of pyrite. PW1PW functional, Lichanot basis set for S and TZVP basis set for Fe were applied for calculations.

Parameter	Optimized structure	Rieder et al., 2007	difference, %
a, Å	5.471	5.416	*1.02*
S-S, Å	2.15	2.16	*-0.46*
Fe-S, Å	2.29	2.26	*1.33*
S-S, Å	3.12	3.08	*1.30*
S-S, Å	3.35	3.32	*0.90*

Table S10. Optimized versus experimental lattice parameter and interatomic distances of marcasite. PW1PW functional, Lichanot basis set for S and ECP_Heifets basis set for Fe were applied for calculations.

Parameter	Optimized structure	Rieder et al., 2007	difference, %
a, Å	4.508	4.446	*1.39*
b, Å	5.516	5.425	*1.68*
c, Å	3.443	3.386	*1.68*
S-S, Å	2.18	2.21	*-1.36*
S-Fe, Å	2.28	2.24	*1.79*
	2.30	2.25	*2.22*
S-S, Å	3.05	2.97	*2.69*
	3.19	3.12	*2.24*

	3.19	3.12	*2.24*
	3.19	3.12	*2.24*
	3.19	3.12	*2.24*
	3.29	3.23	*1.86*
	3.29	3.23	*1.86*
	3.29	3.23	*1.86*
	3.29	3.23	*1.86*
	3.44	3.39	*1.47*
	3.44	3.39	*1.47*

Table S11. Optimized versus experimental lattice parameter and interatomic distances of marcasite. PW1PW functional, Lichanot basis set for S and TZVP basis set for Fe were applied for calculations.

Parameter	Optimized structure	Rieder et al., 2007	difference, %
a, Å	4.482	4.446	*0.84*
b, Å	5.484	5.425	*1.09*
c, Å	3.409	3.386	*0.68*
S-S, Å	2.18	2.21	*-1.36*
S-Fe, Å	2.26	2.24	*0.89*
	2.28	2.25	*1.33*
S-S, Å	3.03	2.97	*2.02*
	3.16	3.12	*1.28*
	3.16	3.12	*1.28*
	3.16	3.12	*1.28*
	3.16	3.12	*1.28*
	3.26	3.23	*0.93*
	3.26	3.23	*0.93*
	3.26	3.23	*0.93*
	3.26	3.23	*0.93*
	3.41	3.39	*0.59*
	3.41	3.39	*0.59*

Table S12. Optimized versus experimental lattice parameter and interatomic distances of arsenopyrite. PW1PW functional, all-electron split-valence Lichanot basis set for S, pp_Heyd basis set for As and ECP _Heifets basis set for Fe were applied for calculations.

Parameter	Optimized structure	Bindi, 2012	difference, %
a, Å	5.714	5.761	*-0.82*
b, Å	5.717	5.684	*0.58*
c, Å	5.737	5.767	*-0.52*
angle β, °	112.31	111.72	*0.53*
As-S, Å	2.36	2.37	*-0.42*
As-Fe, Å	2.38	2.37	*0.42*
	2.39	2.41	*-0.83*
	2.40	2.41	*-0.41*
As-As, Å	3.02	3.04	*-0.66*

	3.18	3.19	*-0.31*
	3.18	3.19	*-0.31*
	3.35	3.35	*0.00*
	3.35	3.35	*0.00*
As-S, Å	3.05	3.06	*-0.33*
	3.05	3.11	*-1.93*
	3.30	3.32	*-0.60*
	3.33	3.33	*0.00*
	3.35	3.33	*0.60*
	3.35	3.38	*-0.89*

Table S13. Optimized versus experimental lattice parameter and interatomic distances of löllingite. PW1PW functional, pp_Heyd basis set for As and ECP_Heifets basis set for Fe were applied for calculations.

Parameter	Optimized structure	Ondrus et al., 2001	difference, %
a, Å	5.224	5.268	*-0.84*
b, Å	6.001	5.963	*0.64*
c, Å	2.86	2.9	*-1.38*
As-As, Å	2.47	2.47	*0.00*
As-Fe, Å	2.35	2.41	*-2.49*
	2.35	2.41	*-2.49*
	2.38	2.37	*0.42*
As-As, Å	2.86	2.9	*-1.38*
	2.86	2.9	*-1.38*
	3.28	3.29	*-0.30*
	3.28	3.29	*-0.30*
	3.28	3.29	*-0.30*
	3.28	3.29	*-0.30*
	3.41	3.4	*0.29*
	3.41	3.4	*0.29*
	3.41	3.4	*0.29*
	3.41	3.4	*0.29*
	3.78	3.81	*-0.79*
	3.78	3.81	*-0.79*
	3.74	3.77	*-0.80*

Table S14. Optimized versus experimental lattice parameter and interatomic distances of dzharkenite. PW1PW functional, pp_Heyd basis set for Se and TZVP basis set for Fe were applied for calculations.

Parameter	Optimized structure	Mandarino, 1995	difference, %
a, Å	5.792	5.783	*0.16*
Se-Se, Å	2.40	2.28	*5.03*
Fe-Se, Å	2.41	2.42	*-0.31*
Se-Se, Å	3.27	3.29	*-0.76*
Se-Se, Å	3.55	3.55	*0.0*

Table S15. TOLINTEG parameter, total energy, cell parameter and volume in single unit cell of pyrite. Basis sets applied for calculations were: Lichanot for S, ECP_Heifets for Fe. PW1PW functional was used for all calculations.

TOLINTEG	Total energy, Eh	Total energy, kcal/mol	*a*, Å	volume, cm^3
Experiment (Rieder et al., 2007)	-	-	5.416	158.87
6 6 6 6 12	-3681.8115	-2310371.6	5.5107	167.35
7 7 7 7 14	-3681.8088	-2310369.9	5.5183	168.04
7 7 7 9 30	-3681.8114	-2310371.5	5.5179	168.00
8 8 8 8 16	-3681.8109	-2310371.2	5.5194	168.14
9 9 9 9 18	-3681.8122	-2310372.1	5.5178	168.00
10 10 10 10 20	-3681.8155	-2310374.1	5.5174	167.95
11 11 11 11 22	-3681.8149	-2310373.7	5.5159	167.82

Table S16. Shrinking factors, k-point density and total energy in supercells 2 x 2 x 2 for pyrite ($Fe_{32}S_{64}$). Basis sets applied for calculations were: Lichanot for S, ECP_Heifets for Fe. PW1PW functional and TOLINTEG 777930 were applied.

Shrinking factor	# k-points	Total energy, Eh	Total energy, kcal/mol	Energy difference, kcal/mol
SHRINK 4 4	14	-29454.49091433	-18482972.10059	-
SHRINK 6 6	40	-29454.49091430	-18482972.10057	0.00002
SHRINK 8 8	90	-29454.49091431	-18482972.10058	-0.00001
SHRINK 10 10	172	-29454.49091432	-18482972.10059	-0.00001
SHRINK 12 12	294	-29454.49091432	-18482972.10058	0.00000
SHRINK 14 14	464	-29454.49091430	-18482972.10057	0.00001
SHRINK 16 16	690	-29454.49091421	-18482972.10051	0.00006
SHRINK 18 18	980	-29454.49091432	-18482972.10059	-0.00007

Table S17. Shrinking factors, k-point density and total energy in supercells 3 x 2 x 2 for pyrite ($Fe_{48}S_{96}$). Basis sets applied for calculations were: Lichanot for S, ECP_Heifets for Fe. PW1PW functional and TOLINTEG 777930 were applied.

Shrinking factor	# k-points	Total energy, Eh	Total energy, kcal/mol	Energy difference, kcal/mol
SHRINK 4 4	36	-44181.73636383	-27724458.146073	-
SHRINK 6 6	112	-44181.73636379	-27724458.146049	0.000024
SHRINK 8 8	260	-44181.73636380	-27724458.146052	-0.000004
SHRINK 10 10	504	-44181.73636379	-27724458.146049	0.000003
SHRINK 12 12	868	-44181.73636379	-27724458.146051	-0.000002
SHRINK 14 14	1376	-44181.73636379	-27724458.146049	0.00000
SHRINK 16 16	2052	-44181.73636380	-27724458.14605	0.00000
SHRINK 18 18	2920	-44181.73636380	-27724458.14605	0.00000

Table S18. Se K-edge absorption energies in eV at the inflection point

Compound	This study[a]	Ryser et al. (2005)	Matamoros-Veloza et al. (2014)[b]
Ferroselite ($FeSe_2$)	12657.2	12657.0	12656.3
Achavelite (FeSe)	12657.4		
Arsenopyrite (FeAsS:Se)	12657.8		
Elemental Se (Se^0)	12658.0	12658.0	12658.0
Marcasite	12658.2		
Pyrite	12658.4		
Na_2SeO_3	12662.2	12662.0	12662.3
Na_2SeO_4	12665.5	12664.0	12665.4

[a]Uncertainty 0.1 eV; [b]Uncertainty 0.4 eV

Table S19. As K-edge absorption energies in eV

Compound	Inflection point	White line energy
Arsenopyrite (FeAsS)	11865.9	11867.6
Pyrite (FeS2)	11866.2	11867.9
Realgar (As_4S_4)	11866.8	11868.4
As_2O_3	11868.6	11870.0
As_2O_5	11872.3	11873.6

Table S20. Calculated lattice parameters

Model	Supercell	*a*, Å	*b*, Å	*c*, Å	α, °	β, °	γ, °
2Se-1	222	10.964	10.964	10.964	90.043	90.043	90.043
2Se-2	222	10.964	10.964	10.964	89.958	90.042	89.958
2Se-3	222	10.964	10.964	10.964	90.000	90.000	89.957
2Se-4	222	10.964	10.964	10.964	90.000	89.995	89.956
3Se-1	322	16.456	10.964	10.964	89.956	90.016	89.985
3Se-2	322	16.456	10.964	10.964	89.958	90.014	89.983
3Se-3	322	16.456	10.964	10.964	89.986	89.986	89.986
3Se-4	322	16.445	10.964	10.964	89.984	89.986	89.985
2As-1	222	11.070	11.042	11.062	89.986	89.941	90.125
2As-2	222	11.075	11.080	11.023	89.705	90.157	90.013
2As-3	222	11.056	11.060	11.060	90.034	90.086	90.061
2As-4	222	11.050	11.066	11.059	90.056	90.356	89.956
3As-1	322	16.589	11.052	11.064	89.962	89.989	90.017
3As-2	322	16.608	11.035	11.071	89.895	89.990	89.926
3As-3	322	16.583	11.056	11.061	90.036	90.077	89.982
3As-4	322	16.586	11.057	11.059	90.016	89.984	90.225
3As-5	322	16.585	11.063	11.056	89.943	90.029	90.072
3As-6	322	16.591	11.059	11.059	89.976	89.977	89.963

3As-7	322	16.580	11.065	11.055	89.899	89.847	89.931
3As-8	322	16.578	11.061	11.056	90.040	90.176	90.137

3. Supplementary figures

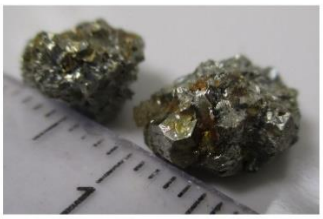

Bolivia (Bol)

Spain (Sp)

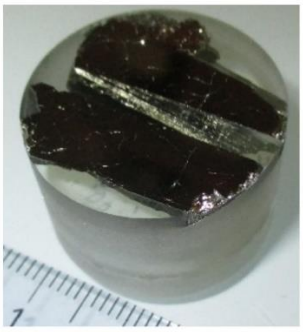

Utah (Ut)

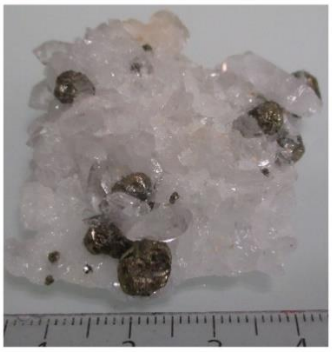

Switzerland (Sw)

Germany (Ger)

Arsenopyrite

Ferroselite

Marcasite

Figure S1. Photographs of pyrite and three references: arsenopyrite (FeAsS), ferroselite (orthorhombic $FeSe_2$), and marcasite (orthorhombic FeS_2).

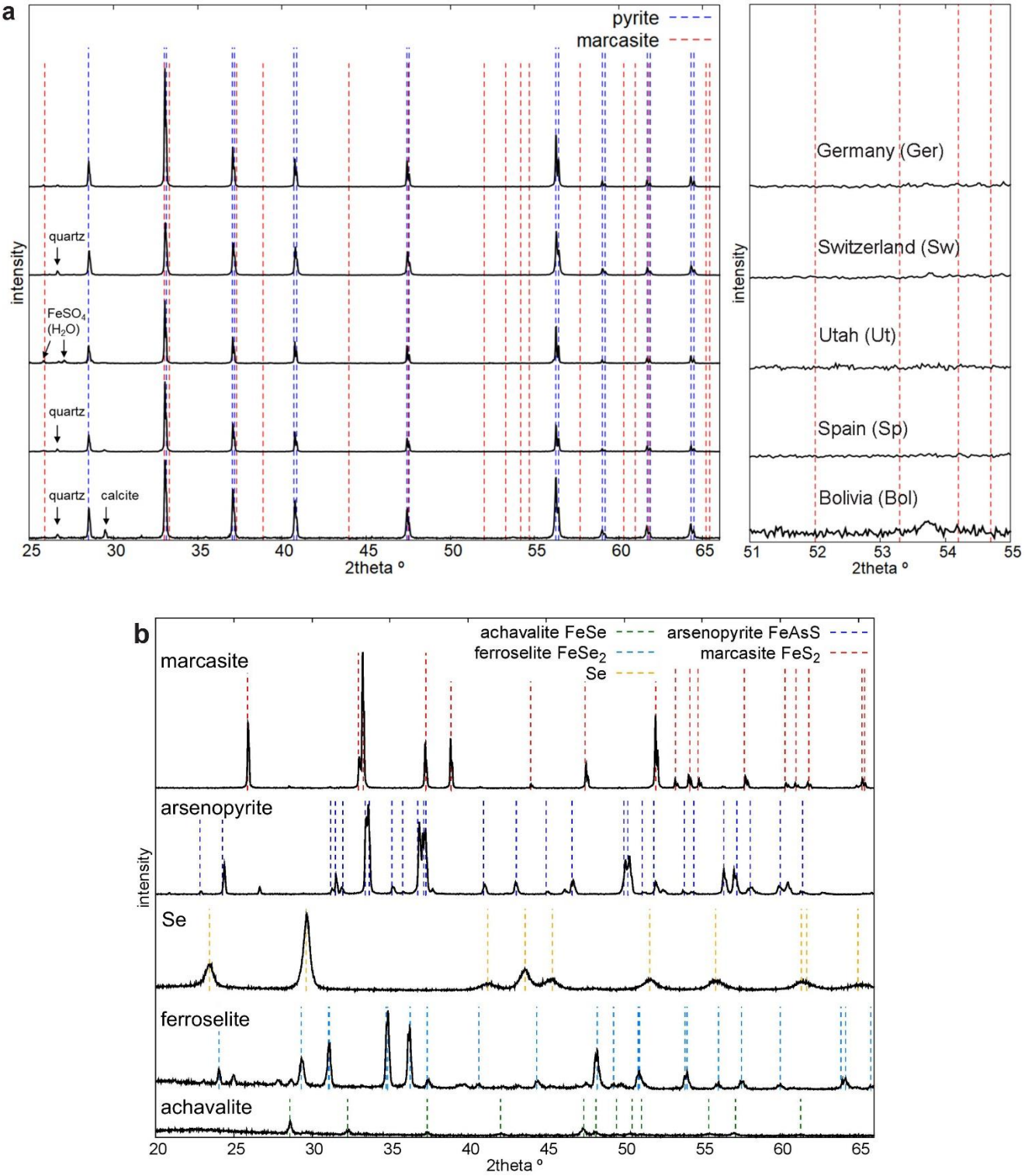

Figure S2. XRD patterns of pyrite (a) and references (b). Blue dashed lines in (a) indicate the reflections of pyrite (cubic FeS_2) and red dashed lines the reflections of marcasite (orthorhombic FeS_2). On the right is an enlargement of the angular region where the second most intense *hkl* reflection of marcasite (211)

occurs (52°) and which does not overlap with any reflection from pyrite. No marcasite impurity is detected in this diagnostic region.

a

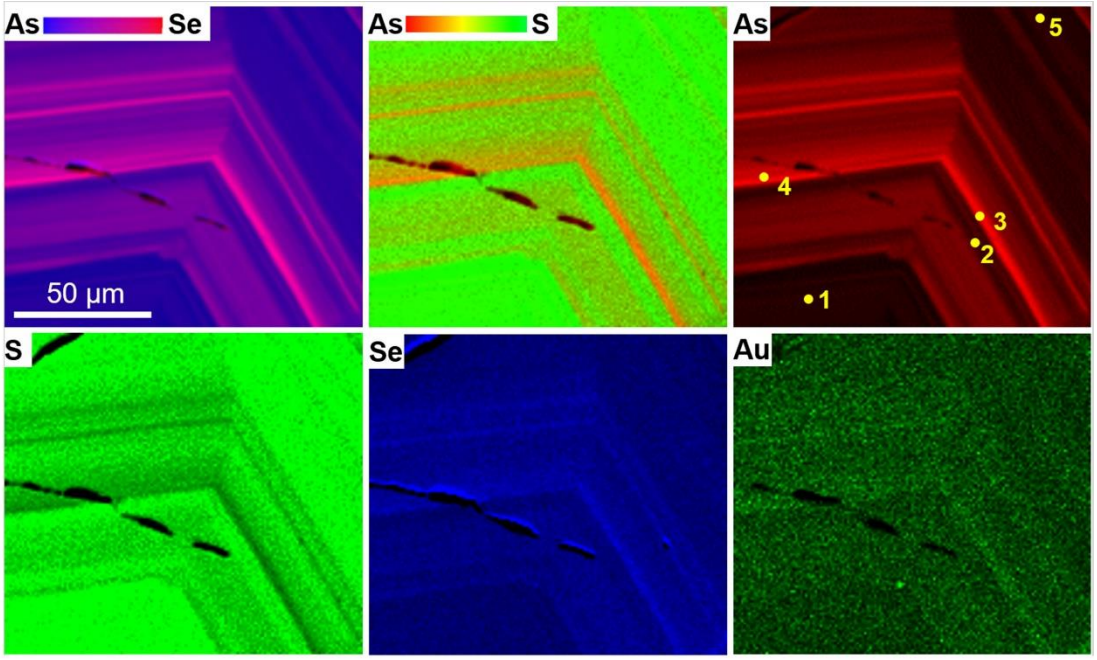

b

	Fe	S	As	Se	Ni	Cu	Zn	Au	Total
Detection limit	-	-	0.0019	0.0014	0.0021	0.0021	0.0021	0.0047	
spot 1	46.39	52.77	0.674	0.006	b.d.l.	0.073	b.d.l.	0.006	99.93
spot 2	46.63	53.32	0.276	0.002	b.d.l.	0.013	b.d.l.	b.d.l.	100.24
spot 3	46.45	52.79	1.072	0.007	b.d.l.	0.011	b.d.l.	b.d.l	100.33
spot 4	46.23	52.94	1.143	0.007	b.d.l.	0.081	b.d.l.	b.d.l	100.41
spot 5	46.60	53.32	0.404	0.004	0.001	0.031	b.d.l.	b.d.l.	100.36

Notes: b.d.l. – below detection limit.

Figure S3. (a) Two color and one color EPMA maps of the distribution of As, Se, S and Au in the zoned pyrite from Bolivia (Bol). Spots with numbers indicate the location of the EPMA analyses. Map size: 115 (V) x 135 (H) μm^2; pixel size: 1 x 1 μm^2; probe diameter: 1 µm; dwell time 2 sec; electron voltage = 20 kV, current = 500 nA. (b) EPMA analyses (wt.%).

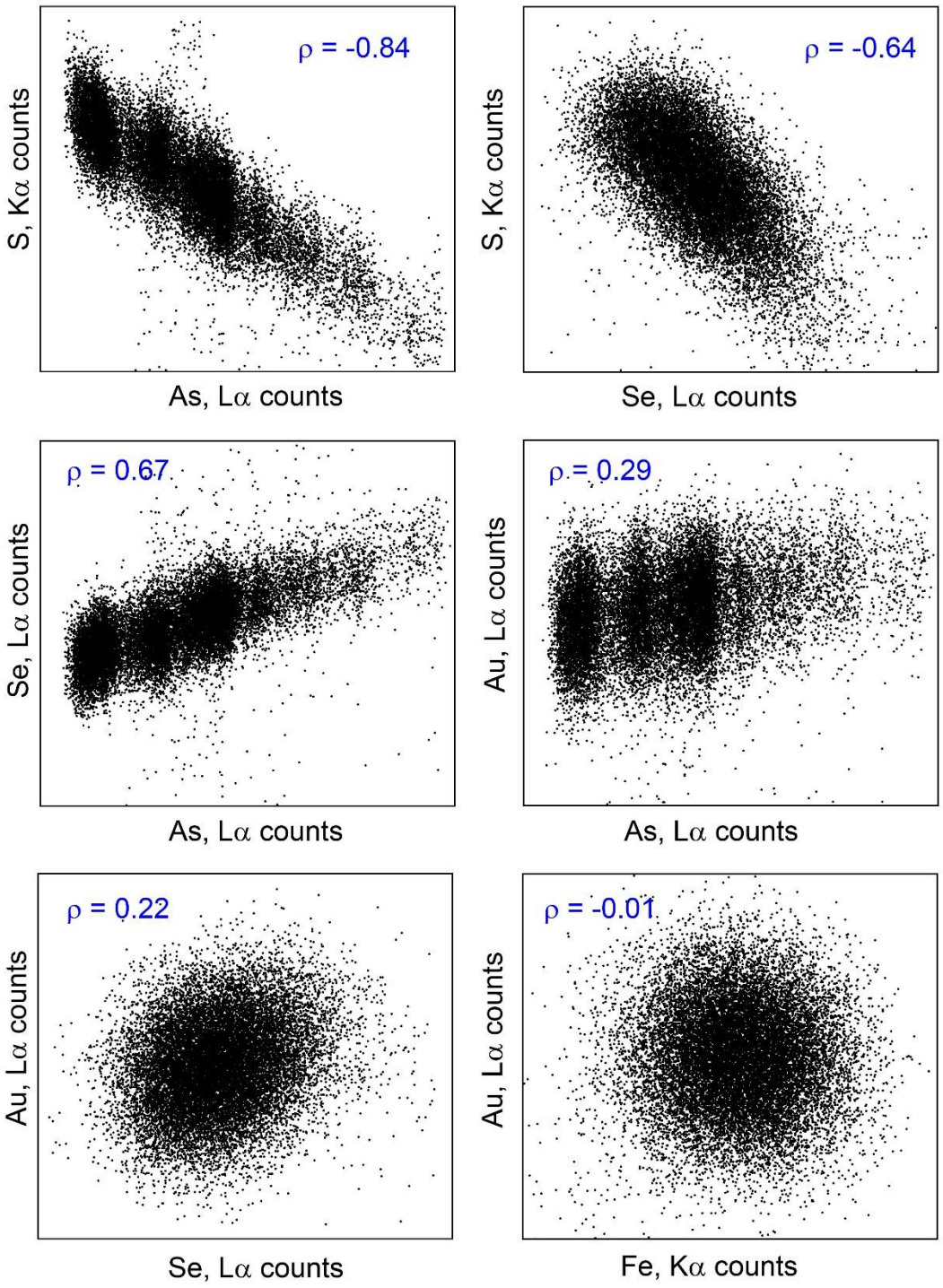

Figure S4. Scatter plots of S, Fe, As, Se, and Au fluorescence counts derived from the EPMA maps of Figure S3 and Pearson correlation coefficients ρ.

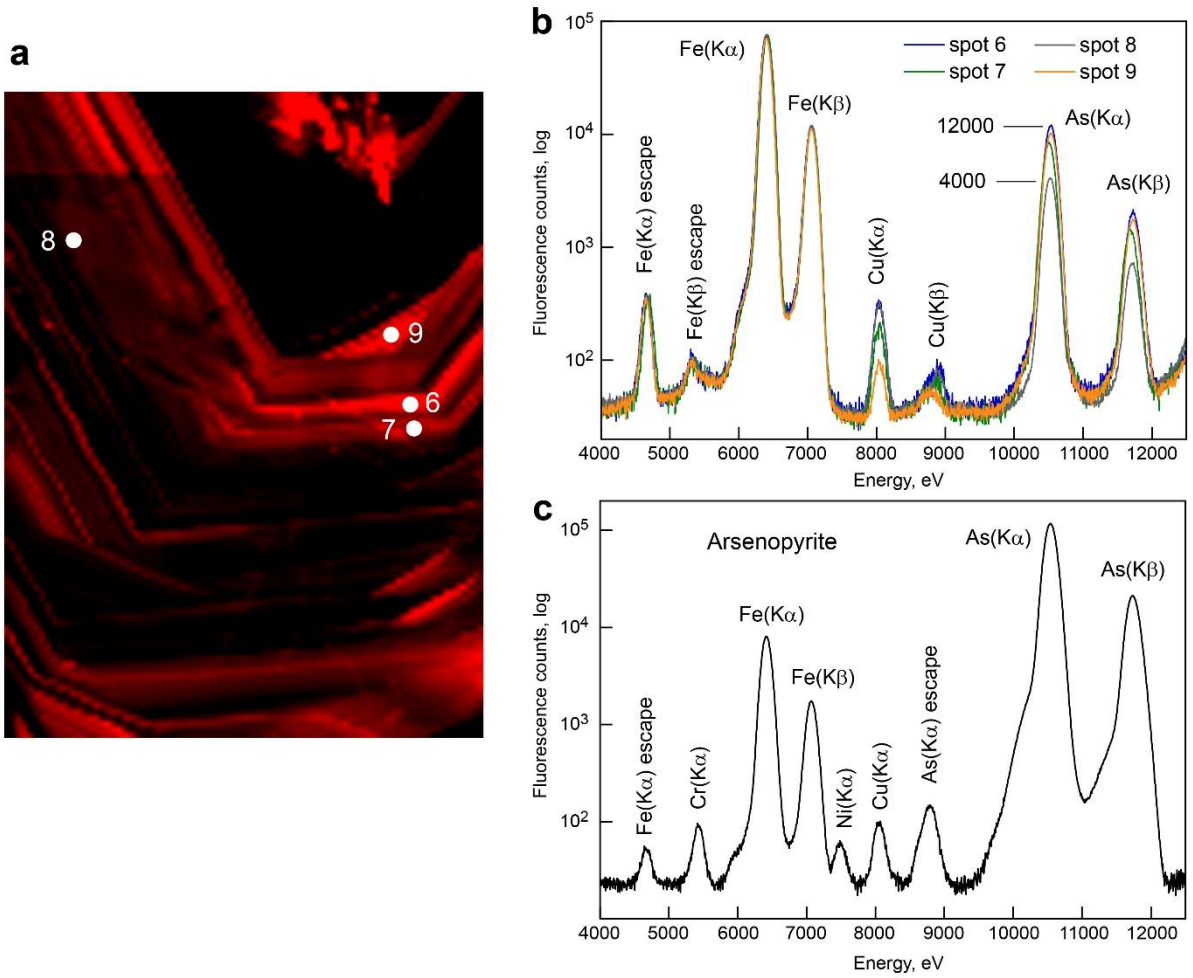

Figure S5. (a) SXRF map of the distribution of As in pyrite from Bolivia (Bol). Map size: 100 (V) x 60 (H) μm^2. (b) Micro SXRF spectra from spots marked 6-9. (c) Bulk SXRF spectrum from arsenopyrite diluted in boron nitride (BN).

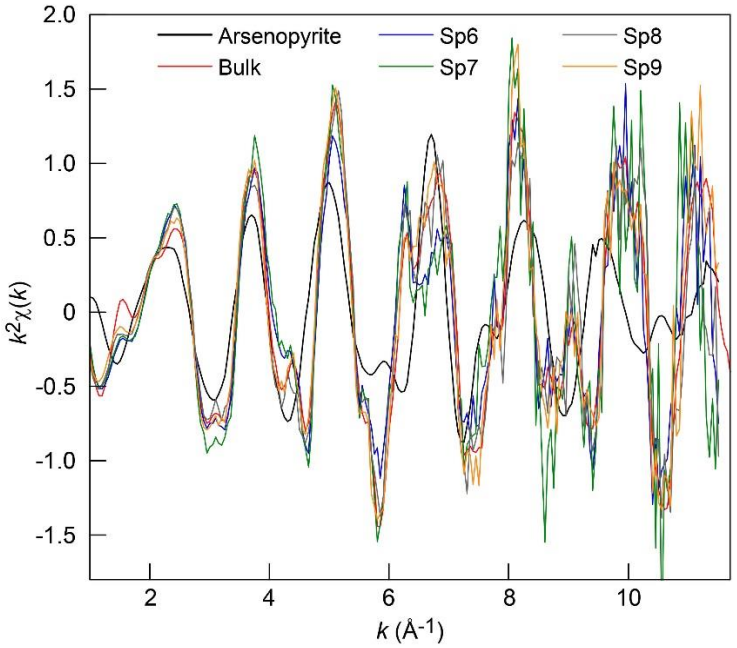

Figure S6. As K-edge micro EXAFS spectra measured on spots 6-9.

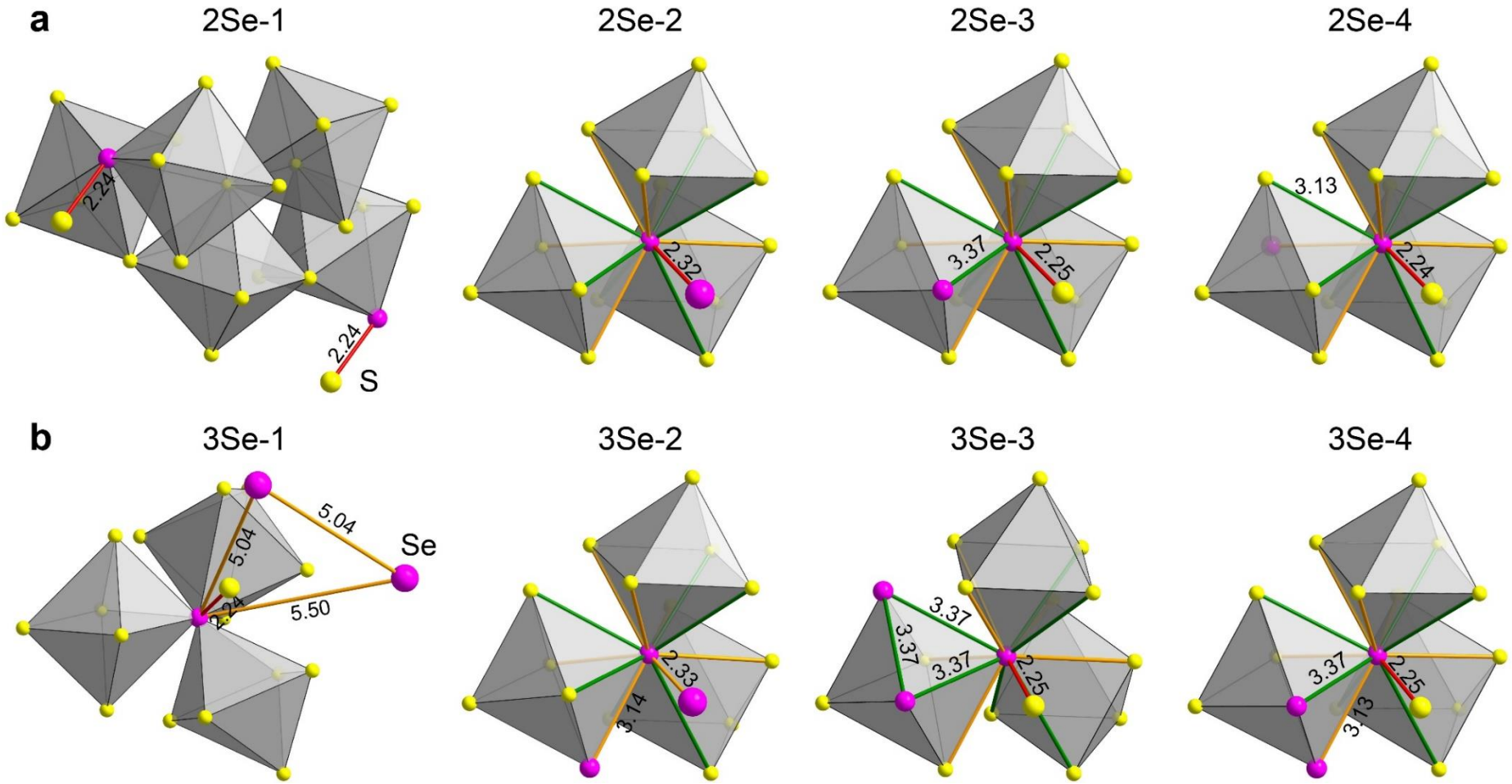

Figure S7. Bonding environment of Se in the $Fe_{32}Se_2S_{62}$ (a) and $Fe_{48}Se_3S_{93}$ (b) equilibrium structures. The S-S edges in yellow are 3.08 Å long and the S-S edges in green are 3.32 Å long in unsubstituted pyrite. The red line connects the dianionic pair. The DFT Se-Se_2 distance of 3.14-3.14 Å on short edges is similar to the EXAFS distance of 3.16 Å for model 2 (Table 2). EXAFS does not have the sensitivity to detect the second Se-Se_2 distance at 3.37 Å on long edges.

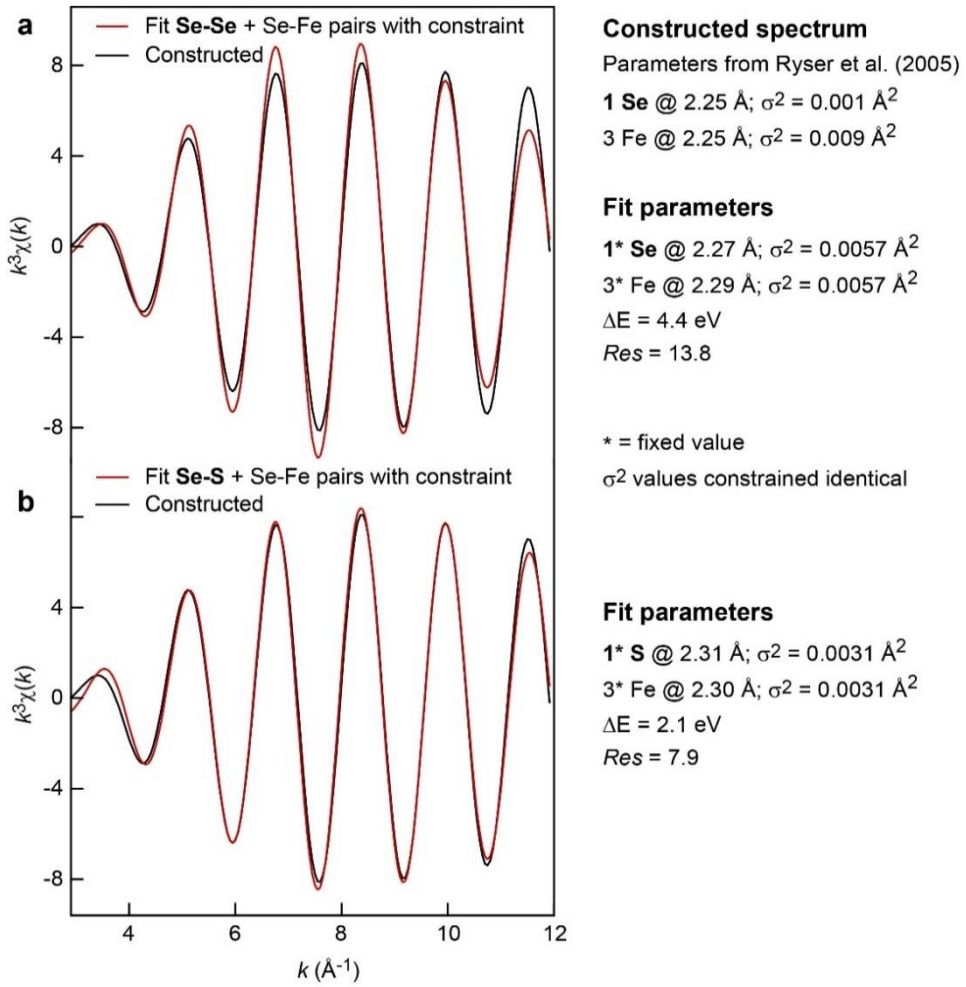

Figure S8. Fit of the first EXAFS shell for sample 2 POI *g* from Ryser et al.[19] The first shell was fit originally with 1 Se at 2.25 Å and 3 Fe at 2.25 Å and the two Debye-Waller factors σ adjusted independently. Data analysis shows that the fit was underconstrained and the coordination number (*CN*) and Debye-Waller (σ) parameters correlated. The EXAFS function was refitted here by covarying the two σ values to suppress correlations. In (a) the first shell contains 1 Se and 3 Fe as in the original fit, and in (b) the Se atom was replaced with S. Results show that the 1S + 3Fe model provides a better fit to data. We conclude from this that $[SeSe]_1$ pairs are unlikely to exist in sample 2 POI *g* and that Se most likely forms a SeS dianion group.

4. Supplementary references

(1) Batanova, V. G.; Sobolev, A. V.; Magnin, V. Trace element analysis by EPMA in geosciences: detection limit, precision and accuracy. *IOP Conf. Ser. Mater. Sci. Eng.* **2018,** *304*, 012001.

(2) Sole, V. A.; Papillon, E.; Cotte, M.; Walter, P.; Susini, J. A multiplatform code for the analysis of energy-dispersive X-ray fluorescence spectra. *Spectrochim. Acta, B* **2007,** *62*, 63-68.

(3) Marcus, M. A.; MacDowell, A. A.; Celestre, R.; Manceau, A.; Miller, T.; Padmore, H. A.; Sublett, R. E. Beamline 10.3.2 at ALS: a hard X-ray microprobe for environmental and materials sciences. *J. Synchrotron Radiat.* **2004,** *11*, 239-247.

(4) Manceau, A.; Marcus, M. A.; Tamura, N. Quantitative speciation of heavy metals in soils and sediments by synchrotron X-ray techniques. In *Applications of Synchrotron Radiation in Low-Temperature Geochemistry and Environmental Science*, Fenter, P. A.; Rivers, M. L.; Sturchio, N. C.; Sutton, S. R., Eds. Mineralogical Society of America: Washington, DC, 2002; Vol. 49, pp 341-428.

(5) Mathon, O.; Beteva, A.; Borrel, J.; Bugnazet, D.; Gatla, S.; Hino, R.; Kantor, I.; Mairs, T.; Munoz, M.; Pasternak, S., et al. The time-resolved and extreme conditions XAS (Texas) facility at the European

Synchrotron Radiation Facility: The general-purpose EXAFS bending-magnet beamline BM23. *J. Synchrotron Radiat.* **2015,** *22*, 1548–1554.
(6) Ravel, B.; Newville, M. ATHENA, ARTEMIS, HEPHAESTUS: data analysis for X-ray absorption spectroscopy using IFEFFIT. *J. Synchrotron Radiat.* **2005,** *12*, 537-541.
(7) Ressler, T. WinXAS: a program for X-ray absorption spectroscopy data analysis under MS-Windows. *J. Synchrotron Radiat.* **1998,** *5*, 118-122.
(8) Ankudinov, A. L.; Rehr, J. J. Relativistic calculations of spin-dependent X-ray-absorption spectra. *Phys. Rev. B* **1997,** *56*, 1712-1716.
(9) Bindi, L.; Moelo, Y.; Leone, P.; Suchaud, M. Stoichiometric arsenopyrite, FeAsS, from La Roche-Balue quarry, Loire-Atlantique, France: Crystal structure and Mössbauer study. *Can. Miner.* **2012,** *50*, 471-479.
(10) Heyd, J.; Peralta, J. E.; Scuseria, G. E.; Martin, R. L. Energy band gaps and lattice parameters evaluated with the Heyd-Scuseria-Ernzerhof screened hybrid functional. *J. Chem. Phys.* **2005,** *123*, 174101.
(11) Anderson, D. G. Iterative procedures for nonlinear integral equations. *J. Assoc. Comput. Mach.* **1965**, 547-560.
(12) Lichanot, A.; Apra, E.; Dovesi, R. Quantum mechanical Hartree-Fock study of the elastic properties of Li_2S and Na_2S. *Phys. Status Solidi B* **1993,** *177*, 157-163.
(13) Peintinger, M. F.; Oliveira, D. V.; Bredow, T. Consistent gaussian basis sets of triple-zeta valence with polarization quality for solid-state calculations. *J. Comput. Chem.* **2013,** *34*, 451-459.
(14) Durand, P.; Barthelat, J. C. Theoretical method to determine atomic pseudopotentials for electric-structure calculations of molecules and solids. *Theor. Chim. Acta* **1975,** *38*, 283-302.
(15) Towler, M. D.; Allan, N. L.; Harrison, N. M.; Saunders, V. R.; Mackrodt, W. C.; Apra, E. Ab initio study of MnO and NiO. *Phys. Rev. B* **1994,** *50*, 5041-5054.
(16) Heifets, E.; Kotomin, E. A.; Bagaturyants, A. A.; J., M. Thermodynamic stability conditions. *J. Phys. Chem. Lett.* **2015,** *6*, 2847-2851.
(17) Heifets, E.; Kotomin, E. A.; Bagaturyants, A. A.; Maier, J. Thermodynamic stability of stoichiometric $LaFeO_3$ and $BiFeO_3$: a hybrid DFT study. *Phys. Chem. Chem. Phys.* **2017,** *19*, 3738-3755.
(18) Wadt, W. R.; Hay, P. J. Ab initio effective core potentials for molecular calculations. Potentials for main group elements Na to Bi. . *J. Chem. Phys.* **1985,** *82*, 284-298.
(19) Ryser, A. L.; Strawn, D. G.; Marcus, M. A.; Johnson-Maynard, J. L.; Gunter, M. E.; Moller, G. Micro-spectroscopic investigation of selenium-bearing minerals from the Western US Phosphate Resource Area. *Geochem. Trans.* **2005,** *6*, 1-11.

6. EXAFS spectra

k^3-weighted As-EXAFS		k^3-weighted Se-EXAFS	
2.0000	0.26616	2.0000	0.79829
2.0500	0.39624	2.0500	0.94560
2.1000	0.49244	2.1000	1.0307
2.1500	0.62861	2.1500	1.0777
2.2000	0.76271	2.2000	1.0826
2.2500	0.98235	2.2500	1.0915
2.3000	1.1905	2.3000	1.1656
2.3500	1.3954	2.3500	1.2407
2.4000	1.5132	2.4000	1.2305
2.4500	1.5907	2.4500	1.1320
2.5000	1.5609	2.5000	0.86891
2.5500	1.4164	2.5500	0.50212
2.6000	1.2083	2.6000	0.13255
2.6500	0.77657	2.6500	-0.26528
2.7000	0.33466	2.7000	-0.76171
2.7500	-0.25579	2.7500	-1.3097

2.8000	-0.78737	2.8000	-1.8355
2.8500	-1.2198	2.8500	-2.2814
2.9000	-1.5274	2.9000	-2.5474
2.9500	-1.6071	2.9500	-2.6568
3.0000	-1.5976	3.0000	-2.6140
3.0500	-1.5973	3.0500	-2.4971
3.1000	-1.6419	3.1000	-2.3552
3.1500	-1.8581	3.1500	-2.1781
3.2000	-2.0263	3.2000	-1.9817
3.2500	-2.1374	3.2500	-1.7655
3.3000	-2.0677	3.3000	-1.3348
3.3500	-1.6056	3.3500	-0.61562
3.4000	-0.69313	3.4000	0.37972
3.4500	0.25093	3.4500	1.5993
3.5000	1.2780	3.5000	2.7271
3.5500	2.0393	3.5500	3.6033
3.6000	2.7763	3.6000	4.2319
3.6500	3.0515	3.6500	4.3552
3.7000	3.1067	3.7000	4.0872
3.7500	3.1547	3.7500	3.8606
3.8000	2.8496	3.8000	3.5537
3.8500	2.0341	3.8500	2.9682
3.9000	1.1905	3.9000	1.7557
3.9500	0.050863	3.9500	-0.21023
4.0000	-0.90771	4.0000	-1.1319
4.0500	-1.5305	4.0500	-2.1138
4.1000	-1.8800	4.1000	-2.9864
4.1500	-2.3348	4.1500	-3.4378
4.2000	-2.5036	4.2000	-3.4491
4.2500	-2.2935	4.2500	-3.5551
4.3000	-2.0885	4.3000	-2.9777
4.3500	-1.6766	4.3500	-2.7266
4.4000	-1.7180	4.4000	-2.6194
4.4500	-2.0713	4.4500	-2.4049
4.5000	-2.6801	4.5000	-2.6267
4.5500	-3.4607	4.5500	-3.3521
4.6000	-3.6702	4.6000	-3.2854
4.6500	-3.4240	4.6500	-3.3018
4.7000	-1.9083	4.7000	-1.4318
4.7500	-0.29493	4.7500	0.17050
4.8000	1.6841	4.8000	1.6898
4.8500	3.4136	4.8500	3.7550
4.9000	4.6399	4.9000	4.6745
4.9500	5.2130	4.9500	5.3861
5.0000	6.1376	5.0000	5.9509
5.0500	6.9637	5.0500	7.0060
5.1000	7.2470	5.1000	6.8002
5.1500	6.9194	5.1500	7.5756
5.2000	5.9423	5.2000	5.8610
5.2500	5.1046	5.2500	5.6884
5.3000	3.5979	5.3000	3.6158
5.3500	2.0693	5.3500	1.2811
5.4000	0.069989	5.4000	0.040582

5.4500	-1.7929	5.4500	-2.3178
5.5000	-3.0620	5.5000	-3.8000
5.5500	-3.5339	5.5500	-4.8479
5.6000	-4.0887	5.6000	-5.0913
5.6500	-4.0167	5.6500	-5.4134
5.7000	-5.3636	5.7000	-5.0293
5.7500	-6.9250	5.7500	-6.5259
5.8000	-8.0400	5.8000	-7.8269
5.8500	-8.2341	5.8500	-7.5178
5.9000	-7.1403	5.9000	-7.0566
5.9500	-5.9404	5.9500	-4.7290
6.0000	-4.2905	6.0000	-3.5815
6.0500	-3.2413	6.0500	-0.90567
6.1000	-1.9562	6.1000	0.84439
6.1500	-0.12405	6.1500	2.5368
6.2000	1.7767	6.2000	3.3244
6.2500	3.0902	6.2500	3.6316
6.3000	3.2769	6.3000	4.3131
6.3500	2.6038	6.3500	2.6509
6.4000	1.7326	6.4000	2.7221
6.4500	2.2010	6.4500	1.4240
6.5000	2.5108	6.5000	2.6028
6.5500	3.7087	6.5500	2.6989
6.6000	3.8455	6.6000	4.1819
6.6500	4.3133	6.6500	3.3907
6.7000	4.8254	6.7000	4.9749
6.7500	5.2282	6.7500	4.4594
6.8000	6.3380	6.8000	6.0585
6.8500	5.9066	6.8500	5.1488
6.9000	5.1261	6.9000	4.5620
6.9500	5.0682	6.9500	2.6317
7.0000	3.8286	7.0000	1.0440
7.0500	2.3723	7.0500	0.74569
7.1000	-0.093105	7.1000	-2.0813
7.1500	-2.8204	7.1500	-2.7736
7.2000	-5.9806	7.2000	-6.8532
7.2500	-7.2432	7.2500	-8.2583
7.3000	-6.8103	7.3000	-7.2454
7.3500	-6.7082	7.3500	-5.4410
7.4000	-7.0758	7.4000	-6.3527
7.4500	-6.9946	7.4500	-6.2466
7.5000	-6.8165	7.5000	-6.1353
7.5500	-6.3441	7.5500	-6.7658
7.6000	-4.6438	7.6000	-4.3765
7.6500	-3.0112	7.6500	-3.7602
7.7000	-2.1338	7.7000	-2.4431
7.7500	-0.76941	7.7500	-2.1632
7.8000	-0.65473	7.8000	-2.1219
7.8500	-1.5031	7.8500	-2.7195
7.9000	-0.18552	7.9000	-1.6914
7.9500	2.1588	7.9500	1.0890
8.0000	6.4714	8.0000	6.1445
8.0500	9.7006	8.0500	9.9183

8.1000	10.657	8.1000	9.9178
8.1500	10.459	8.1500	11.498
8.2000	9.6748	8.2000	9.5717
8.2500	9.3580	8.2500	12.636
8.3000	6.9566	8.3000	8.7415
8.3500	4.7569	8.3500	7.0991
8.4000	1.6793	8.4000	3.2567
8.4500	-1.5539	8.4500	1.1611
8.5000	-3.9910	8.5000	-2.1571
8.5500	-3.5303	8.5500	-2.9457
8.6000	-3.5021	8.6000	-3.1676
8.6500	-3.0120	8.6500	-2.6443
8.7000	-3.6894	8.7000	-1.6841
8.7500	-4.3190	8.7500	-5.3677
8.8000	-5.2845	8.8000	-3.9108
8.8500	-4.7537	8.8500	-4.8447
8.9000	-3.1674	8.9000	-0.25019
8.9500	-1.2276	8.9500	-1.9238
9.0000	-1.8260	9.0000	0.37759
9.0500	-0.56155	9.0500	-0.46755
9.1000	-0.36057	9.1000	-3.1691
9.1500	-2.6416	9.1500	-4.9440
9.2000	-3.8554	9.2000	-8.1887
9.2500	-5.8516	9.2500	-6.3057
9.3000	-6.9440	9.3000	-9.4222
9.3500	-7.0953	9.3500	-11.060
9.4000	-7.0426	9.4000	-10.729
9.4500	-5.6286	9.4500	-6.8438
9.5000	-3.0549	9.5000	-6.1101
9.5500	0.36686	9.5500	0.60362
9.6000	2.8004	9.6000	1.1010
9.6500	6.5784	9.6500	3.4045
9.7000	7.7103	9.7000	9.7957
9.7500	9.4691	9.7500	15.959
9.8000	9.9380	9.8000	16.615
9.8500	9.2164	9.8500	14.028
9.9000	9.5655	9.9000	16.171
9.9500	10.626	9.9500	10.314
10.000	6.9965	10.000	9.6327
10.050	6.6688	10.050	10.408
10.100	5.7293	10.100	7.9521
10.150	7.2677	10.150	9.5880
10.200	5.3881	10.200	7.2901
10.250	3.4387	10.250	0.71264
10.300	-2.2982	10.300	-4.6975
10.350	-5.8703	10.350	-8.5842
10.400	-9.2306	10.400	-13.201
10.450	-11.322	10.450	-13.734
10.500	-12.674	10.500	-17.842
10.550	-13.590	10.550	-16.526
10.600	-14.174	10.600	-17.544
10.650	-13.735	10.650	-16.427
10.700	-11.464	10.700	-11.374

10.750	-8.2448	10.750	-7.0344
10.800	-4.3659	10.800	-4.0859
10.850	-3.2943	10.850	-4.4864
10.900	-0.13950	10.900	-0.25827
10.950	2.9273	10.950	0.34795
11.000	6.5308	11.000	7.5629
11.050	8.1810	11.050	9.1282
11.100	9.1027	11.100	11.082
11.150	9.5960	11.150	8.4138
11.200	8.6832	11.200	9.3127
11.250	9.6212	11.250	7.3250
11.300	9.6674	11.300	14.185
11.350	8.9892	11.350	11.587
11.400	7.4469	11.400	10.299
11.450	3.9599	11.450	7.8726
11.500	0.44762	11.500	3.5633
11.550	-0.95937	11.550	-0.83420
11.600	-2.4085	11.600	-7.1820
11.650	-3.3124	11.650	-7.9555
11.700	-4.5783	11.700	-6.7431
11.750	-3.9655	11.750	-7.1201
11.800	-4.4998	11.800	-4.4345
11.850	-3.0126	11.850	0.56694
11.900	-2.2824	11.900	-0.72288
11.950	-0.048844	11.950	1.1418
12.000	-1.0915	12.000	2.0238
12.050	-3.6917	12.050	0.090986
12.100	-3.2344	12.100	-1.1576
12.150	-3.1282	12.150	-3.3562
12.200	-4.7111	12.200	-5.2304
12.250	-2.3019	12.250	-8.4865
12.300	-1.0214	12.300	-1.5842
12.350	0.32290	12.350	-2.7759
12.400	0.080365	12.400	-4.6243
12.450	-1.5143	12.450	-3.3260
12.500	0.18834	12.500	-5.8521
12.550	1.0020	12.550	-0.85200
12.600	-1.0671	12.600	-0.99685
12.650	-0.032443	12.650	0.10999
12.700	-1.1906	12.700	-2.7454
12.750	1.0653	12.750	2.5813
12.800	3.5748	12.800	-0.55342
12.850	2.4904	12.850	5.3239
12.900	1.2055	12.900	2.9285
12.950	3.1667	12.950	11.961
13.000	4.3522	13.000	9.1107
13.050	6.7235	13.050	12.655
13.100	5.9964	13.100	9.2925
13.150	4.8332	13.150	9.2028
13.200	2.7348	13.200	8.1624
13.250	1.3229	13.250	3.8166
13.300	-0.71824	13.300	7.7472
13.350	-1.3552	13.350	-3.7454

13.400	-2.2247	13.400	-2.7199
13.450	-3.0564	13.450	-2.7324
13.500	-4.0179	13.500	-5.1474
13.550	-5.1273	13.550	-8.8529
13.600	-4.8137	13.600	-5.8019
13.650	-6.1890	13.650	-13.225
13.700	-7.3673	13.700	-13.746
13.750	-6.2048	13.750	-10.505
13.800	-4.6294	13.800	-1.1338
13.850	-5.9750	13.850	-1.2276
13.900	-3.4949	13.900	-6.8623
13.950	0.70274	13.950	-2.9457
14.000	1.1562	14.000	-8.2199
14.050	4.5725	14.050	-4.8167
14.100	4.5363	14.100	-3.4426
14.150	7.1013		
14.200	5.2192		
14.250	5.2430		
14.300	6.3670		
14.350	5.4506		
14.400	2.9672		
14.450	2.1376		
14.500	2.9301		
14.550	2.3790		
14.600	1.1721		
14.650	-1.3919		
14.700	2.0720		
14.750	0.58659		
14.800	1.8174		
14.850	2.3578		
14.900	-4.2839		
14.950	-4.6901		
15.000	-6.2599		
15.050	-5.5322		
15.100	-1.9332		
15.150	-5.1721		
15.200	-7.3530		
15.250	-7.3808		
15.300	-2.1165		
15.350	-2.8451		
15.400	-1.2475		
15.450	-0.82886		
15.500	2.9280		
15.550	1.9028		
15.600	2.5773		
15.650	2.3333		
15.700	0.98683		
15.750	4.6828		
15.800	4.2982		
15.850	2.2402		
15.900	3.5881		
15.950	4.1250		